Greenhouse warming-induced changes in South Asian Summer Monsoon-ENSO teleconnections as modulated by the North Tropical Atlantic

Ajinkya M. Aswale[1,2], Sooraj K P[1], Terray P[3] and Swapna P[1]

[1]Centre for Climate Change Research, Indian Institute of Tropical Meteorology, Ministry of Earth Sciences, Pune 411008, India

[2] Department of Atmospheric and Space Sciences, Savitribai Phule Pune University, Pune, 411007, India

[3]Sorbonne Universites (UPMC, Univ Paris 06)-CNRS-IRD-MNHN, LOCEAN Laboratory, 4 place Jussieu, Paris, France

Corresponding authors address:

Sooraj K. P.

Centre for Climate Change Research, Indian Institute of Tropical Meteorology

Pune 411008, India, https://orcid.org/0000-0003-1246-8922

e-mail: sooraj@tropmet.res.in

Abstract

Recently, the North Tropical Atlantic (NTA) Sea Surface Temperature (SST) anomalies emerge as a key-driver in the biennial transitions of El Niño Southern Oscillation (ENSO) and by extension of the whole ENSO-South Asian Summer Monsoon (SASM) system. In this context, we utilized a suite of Coupled Model Intercomparison Project Phase 6 (CMIP6) models with the Shared Socioeconomic Pathways (SSP2-4.5 and SSP5-8.5) and historical simulations to investigate whether the ENSO-SASM teleconnections as well as its biennial signature undergoes significant modulations in the future warming climate as mediated through the NTA SSTs.

Our results reveal a pronounced increase in NTA variability under greenhouse warming, associated with an enhanced two-way teleconnection between NTA and ENSO, while the increase of ENSO variability is more modest. There is an exaggerated signature for the previous ENSO SSTs impacting boreal spring NTA SSTs, compared to a modest enhancement in NTA forcing on the following ENSO state. However, intriguingly, this later signature of NTA damping the ENSO variability seems to strengthen steadily from the historical simulation to the SSP5-8.5, implying an enhanced NTA forcing and biennial rhythm in future projections. In consonance with this emerging NTA signal, there is a significant increase in the variability of SASM rainfall by 21st century, together with a modest strengthening of the ENSO-SASM relationships in the future warming scenarios. We also noted consistent future strengthening of a biennial signature in the ENSO-SASM teleconnection. It is further inferred that the Pacific equatorial zonal SST gradient in conjunction with the NTA relative warming act as important sources for the future intensification of this biennial signal in ENSO variability and for the inter-model spread in the projections. In contrast to this, the future intensification in SASM rainfall variability and its biennial signature are not uniquely driven by these factors.

Keywords: SASM; NTA; NTA-ENSO-SASM teleconnections; biennial signature; CMIP6 future projections

1. Introduction

The South Asian Summer Monsoon (SASM) is a large-scale phenomenon involving significant ocean-atmospheric interactions and teleconnections. The SASM rainfall governs the Indian agricultural production and the country's economy by accounting for about 80% of India's annual precipitation (Parthasarathy et al. 1994; Katzenberger et al. 2021). Accordingly, the socio-economic well-being of the Indian population is crucially linked to the SASM rainfall variability at different time scales, with the large abnormal behaviour in SASM rainfall often leading to disastrous impacts on many spheres of national activities over this subcontinent, i.e., adversely impacting its agrarian-based economy, health, and food security. The SASM shows a strong sensitivity to Green House Gas (GHG) induced global warming (Kitoh et al. 2013; Sharmila et al. 2015; Sooraj et al. 2015; Chen et al. 2020). As per the recent Intergovernmental Panel on Climate Change Sixth Assessment Report (IPCC AR6), the SASM rainfall is projected to intensify significantly at the end of 21st century, but with enhanced interannual variability implying more floods and droughts in the future (Douville et al. 2021; Katzenberger et al. 2021). Given the complex spatio-temporal characteristics of SASM, the unprecedented enhancement of GHG emissions in the future period could further exacerbate the SASM response at the regional scale. Thus, a robust understanding and projection of the SASM variability are imperative for making detailed management strategies and policies in the future, leading to sustainable developments, and ensuring food and energy security over the SASM region. To achieve this goal, reliable future projections (i.e., at the end of the century) of SASM variability in addition to mean-state changes are crucial.

The SASM interannual variability is influenced by several remote ocean-atmospheric coupled phenomena, including the El Niño Southern Oscillation (ENSO; e.g., Webster et al. 1998), Indian Ocean Dipole (IOD; e.g., Saji et al. 1999), Atlantic Zonal Mode (AZM; e.g., Sabeerali et al. 2019), and North Tropical Atlantic (NTA; Sooraj et al. 2023). In addition to these dominant modes of tropical Sea Surface Temperature (SST) variability, SST variations in the extratropical Pacific (Chattopadhyay et al. 2015) and North Atlantic can also affect SASM interannual variability (e.g., Rajeevan and Sridhar 2008). Thus, the fate of SASM interannual variability at the end of the century consequently relies on the response of these SST modes of climate variability to different future warming scenarios.

The impact of AZM on SASM is well illustrated by several studies, thus suggesting it as an additional driver of SASM variability, beyond ENSO and IOD (e.g., Kucharski et al.

2009; Wang et al. 2009; Sabeerali et al. 2019). However, recent studies showed a weaker AZM-SASM association in the recent period, as AZM and SASM interact with ENSO in a complex manner (Ding et al. 2012; Terray et al. 2023; Sooraj et al. 2023). Furthermore, the AZM-SASM association is projected to weaken in future projections using the latest Coupled Model Intercomparison Project phase 6 (CMIP6) models (Sabeerali et al. 2022).

Recently, there is a growing recognition for the role of NTA (Northern lobe of Atlantic Meridional Mode, AMM; e.g., Chiang and Vimont 2004; Yang et al. 2018, 2021; Cabos et al. 2019) as a key driver of the ENSO biennial system (Ham et al. 2013a, b; Wang et al. 2017). The NTA SST anomalies generally peak in boreal spring (March to May, MAM) and are dominantly forced by ENSO and the North Atlantic Oscillation (NAO), with a surface wind-evaporation feedback contributing to their further development (e.g., Yang et al. 2018, 2021). The NTA SST as enforced by ENSO can in-turn fasten the demise of ENSO events in the following year through its capacitor effect, thus acting as a key driver of ENSO biennial rhythm (Wang et al. 2017). Consequently, NTA SSTs emerged as an important driver of the whole ENSO-SASM system during recent decades (Yang and Huang 2021; Terray et al. 2023; Sooraj et al. 2023).

Moreover, Sooraj et al. (2023) have recently demonstrated that the NTA has a significant influence on the SASM variability. They illustrated the key role of NTA SSTs in the reversal of the ENSO conditions through the capacitor effect, but also in modulating the interannual variability of SASM as mediated by ENSO. Further, their coupled sensitivity experiments revealed the asymmetric response in the simulated NTA-ENSO-SASM association as the cold NTA perturbations (imposed on strong La Niña initial conditions) show a significantly stronger anomalous boreal summer SASM rainfall response than the warm NTA perturbation experiments (using strong El Niño initial conditions).

In light of the above, it thus transpires that the NTA SSTs are an important driver of the whole ENSO-SASM system. However, one can envisage the following unresolved questions. Whether the recent NTA-SASM association through ENSO is reinforced by anthropogenic forcing or by natural variability? As the NTA impact on SASM is mainly mediated through ENSO, does it mean that the role of NTA will also be weaker if the ENSO-SASM weakens in the future projections (Goswami and An 2023)? On the other way around, if the ENSO-SASM relationship is stronger in the future projections, will that be partly attributable to NTA mean state and variability changes? Finally, whether the biennial rhythm of ENSO-SASM teleconnections can undergo significant modifications in the future projections as modulated through NTA?

A comprehensive analysis addressing the above questions is missing so far to the best of our knowledge, thus defining the focus of the present study. Such an investigation assumes further significance in the backdrop of the projected weakening of AZM-SASM association in future warming projections (Sabeerali et al. 2022). Moreover, as the NTA SST is modulating the ENSO-SASM association non-linearly (Sooraj et al. 2023) and as the NTA and ENSO variabilities are projected to increase in the future (e.g., Cai et al. 2018, 2021; Fredriksen et al. 2020; Yang et al. 2021), a comprehensive evaluation of the NTA-ENSO-SASM teleconnections in a future warming scenario is warranted. These considerations lead to the present study focusing on the NTA-ENSO-SASM teleconnection in future scenarios using a consortium of CMIP6 coupled models.

The manuscript is arranged in the following way. Section 2 outlines the observed and CMIP6 datasets, and the methodology adopted. The NTA variability and its associated teleconnection with SASM and ENSO in recent observations and historical simulations are described in Sections 3 and 4, respectively. Sections 5 and 6 detail the projected changes in NTA-ENSO-SASM teleconnection in the future. Section 7 explores the plausible origin of the stronger projected biennial signature of the NTA-ENSO-SASM system. Section 8 contains the summary and concluding remarks.

2. Data and methods

2.1 CMIP6 simulations

The study used the historical and Shared Socioeconomic Pathways (SSPs) scenario climate experiments from 30 coupled models contributing to CMIP6 (Eyring et al. 2016; O’Neill et al. 2016). For SSPs, we considered SSP2-4.5 (a medium-forcing scenario, “middle□of□the□road” pathway) and SSP5-8.5 (a highest-forcing scenario, “high-end-of-the-road” pathway). Table 1 provides a general overview of the model datasets. The historical runs of CMIP6 models are forced with the natural and anthropogenic forcings (Eyring et al. 2016), while the SSP2-4.5 (SSP5-8.5) scenario depicts the medium (highest) emission scenario where the radiative forcing reaches 4.5 W/m^2 (8.5 W/m^2) by the end of the 21st century (O'Neill et al. 2016). Note that these two SSPs will be hereafter simply referred to as SSP245 and SSP585, wherever appropriate. Note also that we have restricted our analysis to the first available ensemble member (i.e., either r1i1p1f1 or r1i1p1f2) from each model.

2.2 Observational Data

We used monthly SST reanalysis from Hadley Centre Sea Ice and Sea Surface Temperature dataset version 1.1 (HadISST v1.1, Rayner et al. 2003) from 1948 to 2020. Secondly, we used a global monthly mean precipitation dataset with a horizontal resolution of 2.5°×2.5°, as obtained from the Global Precipitation Climatology Project (GPCP) monthly precipitation analysis for the period from 1979 to 2020 (Adler et al. 2018). Additionally, we used the gridded high resolution (0.25° × 0.25°) regional precipitation dataset from the India Meteorological Department (IMD; Pai et al. 2014) as available for the period from 1948 to 2020.

2.3 Methodology

We used the same length of time period (42 years) for both the observations (1979–2020) and CMIP6 model simulations for the analysis. While the historical simulations used the period of 1973–2014, the SSP scenarios used the period 2058-2099. The monthly datasets from both the observation and CMIP6 models are bilinearly interpolated into a 1° × 1° grid for ease of comparison. Also, all datasets (as applied to the historical and SSPs separately) are linearly detrended, and the climatological mean is removed prior to the analysis as our focus is on interannual variability.

2.3.1 NTA, Niño3.4 and SASM indices

To identify the NTA variability in the observation and the CMIP6 models (for both the historical and future simulations), Empirical Orthogonal Function (EOF) analysis is carried out on the linearly detrended boreal spring (MAM season) SST anomalies over the NTA region (0° to 30°N and 70°W to 10°W). A basin-wide mode consistently emerges as the first mode of EOF analysis (EOF1) in both historical and SSPs (see Fig. 3b-d), similar to the observed results in Figure 3a (Sooraj et al. 2023). Thus, in order to define warm (cold) NTA events, we have used a NTA index based on the first Principal Component (PC1, as corresponding to EOF1) time series, for both the historical and SSPs. Then, in the historical simulations, warm (cold) NTA events are identified based on the threshold of 1 Standard Deviation (i.e., SD at interannual time scale), as calculated for the MAM season. Next, the Niño3.4 index is defined as the area average of SST anomalies over the 5°S to 5°N and 170°W to 120°W to identify the El Niño (La Niña) events which are greater than or equal to 1 SD (less than or equal to -1 SD), as corresponding to the boreal winter period [December to February]. It is important to note that the same SST thresholds, as used to identify the NTA and ENSO events in the historical simulations, are retained for the identification of events in the future simulations (SSPs) in order to depict accurately the changes of variability and teleconnections. Finally, the SASM rainfall time series is defined as rainfall anomalies averaged over the Indian land points between 10°N to 30°N and 70°E to 95°E and for the boreal summer (June to September, JJAS).

While identifying events in selected CMIP6 models (see Section 2.3.2 for the details on the model selection), it is also ensured that the identified ENSO events develop in JJAS(0) following the NTA events in MAM(0) thus attaining the ENSO peak in the subsequent boreal winter season [D(0)JF(1)]. It is found that most of these selected NTA events are in-turn induced by the previous ENSO during D(-1)JF(0) (figure not shown), as consistent with the observed biennial nature of ENSO. Note that hereafter "1" refers to the following year, while "-1" represent the preceding year of current year 0 during which NTA events emerge in MAM season.

In order to ascertain the inter-model spread in ENSO variance, we have also performed EOF analysis over the Pacific region (110°E-70°W, 30°S-30°N) for all the 30 models with an intention to see their ability in capturing the ENSO variance and pattern (as explained by the dominant EOF mode, EOF1) during boreal winter period [December to February]. Our results show that all the 30 models show fidelity in capturing the dominant ENSO variance statistics (Figure not shown).

It is well-known that the ENSO is the main driver of NTA (Yang et al. 2018, 2021; Terray et al. 2023; Sooraj et al. 2023). But the precursory nature of NTA in hastening the ENSO transition is emerging during the recent decades taking the form of a biennial rhythm involving both ENSO and NTA (see Introduction and Section 3). This justifies our above choice of defining composites using the above identified co-occurring NTA-ENSO events with an intention to better characterize the modulations of this biennial NTA-ENSO rhythm in the projections. The observed composite analysis focussing on such co-occurring NTA-ENSO events is documented in Sooraj et al. (2023) and hence the same analysis is not repeated here for brevity, and we will focus mainly on the changes of the composites across future scenarios.

2.3.2 Models Selection Procedure

Analyses of current generation of coupled models as participated in CMIP6 show improved performance in simulating the observed SASM rainfall climatology and variability compared to the previous generation of models from CMIP3 to CMIP5 (Rajendran et al. 2022; Choudhury et al. 2021; Guilbert et al. 2023). However, the current CMIP6 coupled models still show prominent biases in simulating the observed climate statistics (both mean and variability). So before analysing the future projections from CMIP6, a detailed evaluation on the fidelity of the current state-of-the-art coupled models to capture the present-day climatology and variability aspects of the NTA-SASM system is attempted here using all 30 CMIP6 models thus facilitating us to select a set of models showing better agreement with observations. In this direction, we implemented Taylor diagrams (Taylor 2001) to assess the performance of the CMIP6 models (see Fig. 1a-c) in replicating the present-day climate statistics for the NTA SST and SASM rainfall. Note here that the reference climate statistics of the NTA SSTs are derived from the HadISST, while the observed rainfall statistics are estimated from the GPCP rainfall dataset. Fig. 1 obviously shows large inter-model spread in climate statistics for both the NTA SST and Indian land rainfall. Considering this large spread, optimally best models are selected based on the following criteria:

1. Pattern Correlation Coefficient (PCC) for the EOF1 of SST (as described earlier) of the boreal spring season (MAM) over the NTA region, against the corresponding HadISST observation, is greater than or equal to 0.5 (based on Fig. 1a)
2. The PCC for mean summer monsoon rainfall over the Indian land points, against the corresponding GPCP observation, is greater than or equal to 0.5 (based on Fig. 1b)
3. The PCC for the interannual variability in summer monsoon rainfall over Indian land points, versus the equivalent GPCP observation, is more than 0.7 (based on Fig. 1c)
4. The spatial standard deviation ratio is between 0.75 and 1.20. Here note that the standard deviation for each model is averaged spatially for the above 3 criteria (i.e., EOF1 in SST, mean and variability in rainfall) and subsequently expressed as ratio between the model and observed standard deviation estimates.

We identified 11 CMIP6 models (as highlighted in bold, see Table 1) for the assessment of the NTA-ENSO-SASM teleconnection, that adequately replicate both the observed NTA SST variability and climatology/variability of SASM rainfall during the recent decades. In other words, they show improved skill in reproducing the dominant EOF pattern of SST over NTA (Yang et al. 2021) and in replicating the JJAS mean rainfall climatology across the Indian landmass along with its interannual variability (Choudhury et al. 2021; Rajendran et al. 2022. Note that, the model NESM3 exhibits an unrealistic out-of-phase relationship between NTA SST and SASM rainfall in future simulations (both in SSP425 and SSP585, figure not shown) though it realistically captured the observed in-phase relationship in the historical simulations and consequently we have removed it from the selected list of the "best" models. Accordingly, there are 10 selected models (highlighted in bold, see Table 1), as subsequently employed it for deeper analysis on future projections on NTA-ENSO-SASM. However, we will also verify our main results using all 30 CMIP6 models (see Table 1) in order to test the robustness of our results and, thus, strengthen our conclusions. The results based on the 10 selected models will be referred to as hist_10m, while those using 30 models are referred simply as historical, wherever appropriate. Similar conventions are applicable for the future simulations as well (i.e., ssp245_10m, ssp585_10m, ssp245 and ssp585). Also, the multi-model ensemble means (MME) of 10 selected and all 30 CMIP6 models are referred, respectively, as MME10 and MME30, wherever appropriate.

2.3.3 Statistical Significance

In order to assess the statistical significance of the future change in different climate statistics (i.e., mean, variability etc.) compared to the historical simulations, bootstrap (more precisely resampling tests without replacement) tests are performed (Noreen 1989; Terray et al. 2003). The procedure allows for testing the null hypothesis that two samples (here historical simulations and projections) are drawn from the same (finite) population. The difference in statistics between the two groups of samples is used to assess their chance of occurrences under the null hypothesis based on randomization tests with 10000 shuffles in a finite-population framework, which follows the methodology described in Terray et al. (2003).

Similar bootstrapping procedures, as described above, are additionally employed to assess the statistical significance of the future changes in the NTA-ENSO composites (i.e., the difference in the composites between future and historical). Finally, a similar bootstrap test is further performed to assess the statistical significance of the correlation maps (Noreen 1989).

3. Emerging NTA-ENSO-SASM teleconnection in recent decades

As the NTA has a profound impact on SASM through ENSO during recent decades (following the prelude), one will be curious to ascertain how this strengthened teleconnection emerges in the backdrop of the global warming and also the relative warming of the NTA compared to the whole Tropics in observations.

Figure 2a shows the 21-year sliding correlation analysis between pre-monsoon [e.g., MAM(0), as noted earlier "0" refers to the current year] NTA SST anomalies and boreal summer SASM rainfall [e.g., JJAS(0)] from 1948 to 2020 (blue line in Fig. 2a). A weak positive association between NTA SST and SASM rainfall is observed until 1995, growing stronger in the following years thus attaining significance in the 2000s. Coinciding with this, the 21-year sliding correlations between the MAM(0) NTA SST and JJAS(0) ENSO indices (see green line in Fig. 2a) are also steadily increasing in amplitude after the 1995s. This stronger positive association between NTA and SASM rainfall and the reverse NTA-ENSO association conspicuously suggest stronger and significant teleconnection pathways linking NTA to SASM as mediated by ENSO consistent with the results of Yang and Huang (2021) and Sooraj et al. (2023). Figure 2a (red line in Fig. 2a) further reveals that the inverse association between ENSO and SASM has also strengthened after 2000, thus indicating a renewal of the ENSO-SASM teleconnection. According to Yang and Huang (2021), this indicates a new interdecadal transition in the ENSO-SASM system. This also suggests the hypothesis that the enhanced NTA impact on ENSO variability after 1995s (green line in Fig. 2a) may be one of the reasons of the observed recovery of the ENSO-SASM relationship in the 21st century (red line in Fig. 2a).

A 21-year moving average as applied to the time series of NTA SST anomalies further demonstrates that the NTA experienced pronounced warming after 1995, while below-normal SST anomalies dominate before (Fig. 2b). Moreover, the tropical SST anomalies, as averaged over 30°S to 30°N and 180°W to 180°E (black line in Fig. 2b), show that the entire Tropics are warming at a slower rate compared to the NTA warming, during the recent decades (i.e., after 2000) suggesting that the NTA is very susceptible to anthropogenic changes. Sooraj et al. (2023) also recently made a similar inference that the NTA is warming faster than other tropical oceans (i.e., tropical Pacific and Indian oceans). Park et al. (2022) also observed this pronounced NTA warming after 1995 and suggested that this warmer NTA basic state created conditions favourable for NTA to efficiently impact the ENSO transitions in the recent decades (Wang et al. 2017) coinciding with the above results.

Given this emerging teleconnection between NTA, SASM and ENSO and its possible link to the relative warming of the NTA compared to the whole Tropics in the recent decades (Fig. 2), we explore in the next Sections how these teleconnections evolve in future warming scenarios using CMIP6 coupled models.

4. NTA-ENSO-SASM teleconnection in the historical simulations of CMIP6

Before proceeding with a deeper analysis using only selected models, we performed here a correlation analysis between different indices (e.g., Niño3.4, NTA and SASM as defined in Section 2) using observational datasets and historical simulations from all 30 CMIP6 models to assess the performance and spread of the CMIP6 models in simulating the ENSO, NTA and SASM system and validate our model selection procedure (Fig. 1d). Note that the selected 10 models are highlighted in gray shading in Figure 1d for easy interpretation.

Previous studies have shown that there are strong two-way interactions between the NTA and ENSO (e.g., Cai et al. 2019; Terray et al. 2023; Sooraj et al. 2023). As demonstrated by Fig. 1d, the previous ENSO state (during the preceding boreal winter) enforces the NTA SSTs as revealed by the observed positive association between Niño3.4 SST [D(-1)JF(0)] and NTA PC1 [MAM(0)] indices, thus coinciding with earlier studies (Jiang and Li 2019; Park and Li 2019; Terray et al. 2023; Sooraj et al. 2023, see red bar in Fig. 1d). All the 30 coupled models (in particular the selected 10 models) realistically simulate this lag relationship of NTA MAM(0) SST anomalies to the previous ENSO state (i.e., ENSO impacting NTA) and many models obviously exaggerate this ENSO forcing on the NTA.

The ENSO induced NTA SST anomalies can in-turn impact the ENSO transition through its capacitor effect thus maintaining the ENSO biennial rhythm (e.g., Ham et al. 2013a, b; Wang et al. 2017; Park et al. 2022, 2023; Sooraj et al. 2023). This is manifested by an inverse relationship between the NTA PC1 index [MAM(0)] and the Niño3.4 SST index [D(0)JF(1)] in both observations and CMIP6 models (green bars in Fig. 1d). But only 19 (out of 30) CMIP6 models are able to capture realistically this NTA impact on the following ENSO with rest of the models fail to achieve it. Recently, Park et al. (2022) has also noted that the strength of NTA impact on ENSO varies widely across the CMIP5 models. In summary, the current models overemphasize the ENSO forcing on NTA rather than the reverse. This is attributed to the intensity of the climatological subtropical North Pacific high as according to Park et al. (2022) the NTA triggering on ENSO is proportional to the strength of the Pacific subtropical high in the models. Note that this may also be partly associated with the bias in tropical Atlantic mean state according to Terray et al. (2023).

Next, we examined a similar correlation analysis between JJAS(0) Niño3.4 SST and SASM rainfall, as it is crucial to validate the observed inverse association between ENSO and SASM rainfall in the CMIP6 historical simulations. All 30 CMIP6 models exhibit an inverse relationship between Niño3.4 SST and SASM rainfall though with a large inter-model spread in amplitude (see blue bars in Fig. 1d). Then we looked for the lagged association between the NTA PC1 and the SASM rainfall indices which as per the observation shows a positive relationship, thus suggesting the strengthening (weakening) of SASM rainfall during the positive (negative) NTA events (Sooraj et al. 2023, see violet bars in Fig. 1d). Interestingly, all the selected models are able to capture this observed positive association between NTA SST and SASM rainfall though some of it are slightly underestimating it. But, more importantly, rest of the models (i.e., 17 models out of 20) simulate mostly inverse associations (contrary to the observed association) and are thus unable to replicate the observed interannual relationship, a feature which validate our selection procedure.

During boreal spring, the observed dominant EOF pattern in SST shows significant anomalous large-scale warming (or cooling) over the NTA region (i.e., maximum warming occurring over the regions 10°N to 25°N) with SST anomalies of opposite polarity to its northwest (Fig. 3a). Figure 3b shows the MME in dominant EOF SST patterns for the selected 10 CMIP6 models (i.e., MME10) in historical simulation. The selected models demonstrate similar observed anomalous large-scale SST patterns over NTA region (with a pattern correlation of 0.84 for MME10) but with a weaker amplitude (Fig. 3b). Thus, the leading EOF mode of spring NTA SST anomalies as simulated by the selected models is well consistent with the observed features. Interestingly, the weaker coherency and amplitude of the NTA anomalies despite of the stronger ENSO forcing in the models may also partly explain the subsequent reduced NTA forcing on ENSO in the models (as illustrated in Fig. 1d) in addition to the potential role of the subtropical North Pacific high (Park et al. 2022).

Next, to envisage the associated pattern of rainfall over the SASM region (in particular over Indian landmass), regression analysis is further carried out between the NTA PC1 index and JJAS averaged rainfall in observations and simulations. The MME of the selected models (MME10) shows significant positive rainfall anomalies over Peninsular India extending to central India similar to the observation (Fig. 3e and 3f). In a broader sense, we find that our selected models are able to replicate the observed positive linkage between NTA SST and SASM rainfall (with a pattern correlation 0.64 for MME10).

To sum up, the selected models in their historical simulations share many features with those in observations and thus are capable of reproducing the observed relationships during recent decades (e.g., Fig. 1d).

5. Increased NTA-ENSO association in the future global warming scenario

Similar to the historical period, we then performed the EOF analysis on the linearly detrended boreal spring season NTA SST anomalies (see Section 2), over the future period from 2058 to 2099 for the selected 10 CMIP6 models using their SSP245 and SSP585 scenarios. We show the dominant EOF SST patterns of the MME of the 10 selected models (MME10) in Figures 3c-d. The MME10 projects a notable increase in NTA anomalies in the future warming climate, in particular for the SSP585 scenario, as compared to the historical period (compare Fig. 3b with Fig. 3c and 3d), yet the explained variance by the first EOF is still lower than in observations even for the SSP585 scenario. However, these variances described by the first EOF mode also show a clear increase from historical to both SSPs (see Fig. 4a and the figure caption for more details). The MME10 (MME30) show an ensemble mean increase of 8% (4.45%) in ssp245_10m (ssp245), while it is 9.5% (4.3%) for ssp585_10m (ssp585). The ensemble mean increases for the explained variances (for both MME10 and MME30) are further statistically significant according to a bootstrap test (see Figs. 4c, S1a). Similar significantly projected ensemble mean increase is obvious in NTA SD as well (based on bootstrap test, see Figs. 4b-d, S1b). So, the increase in the NTA EOF variance and the NTA SD is not only observed for the selected models, but also for all the 30 models, hence implying that NTA variability show a general increase in the future scenarios irrespective of model selection or choice of the NTA index (see Fig. S1a, b; Yang et al. 2021).

As the NTA variability is prominently linked to ENSO variation in the models (Fig. 1d), it prompted us to examine the ENSO SD signature in the future warming scenarios (see Fig. 5a). As per our analysis, the MME10 (MME30) of Niño3.4 SD is 1.05 (1.15), 1.21 (1.22), and 1.24 (1.23) °C, as observed in the hist_10m (historical), ssp245_10m (ssp245), and ssp585_10m (ssp585), respectively (Fig. 5a). Comparing these values to the historical period, we observe a percentage increase of 15% (5.6%) and 18% (6.8%) in the MME10 (MME30) for ssp245_10m (ssp245) and ssp585_10m (ssp585), respectively. Importantly, these ensemble mean projected increases are also statistically significant according to a bootstrap test (see Figs. 5c, S1c). These results suggest that the ENSO variability also increases slightly in a warming climate, though a recent study indicated a lack of consensus within CMIP6 models on the change in variance and spectra of ENSO (Fredriksen et al. 2020). However, this increase is obviously less marked than in our NTA index highlighting the need of further analyses on the role of NTA in future NTA-ENSO-SASM teleconnections.

Given this systematic and significant increase of NTA SST variability in the future simulations, it is intuitive to first examine the status of NTA-ENSO association in the future climate. This is done in Figure 6a through the lead-lag correlations between the NTA PC1 index and monthly time series Niño3.4 SST for observation, historical (blue line), SSP245 (red line) and SSP585 (orange line) scenarios. Note, both for historical and SSPs, the correlations are computed for each selected model and presented finally as an ensemble mean (MME10). The observed lead-lag relationship is reproduced in the historical scenario with maximum positive correlation one year before the NTA index and then gradually weakening in the early boreal spring of year 0, reversed in sign during the pre-monsoon season of year 0 and, thus, eventually attaining significant negative correlation values in boreal summer of year 0 and the subsequent seasons. Basically, similar to observation, the selected CMIP6 models also illustrate that the NTA events are dominantly forced by previous ENSO state (during year -1) which in-turn may play a role in transitions from El Niño to La Niña states as the NTA events in the boreal spring season [MAM(0)] are inversely and significantly associated with subsequent ENSO [D(0)JF(1)] events in the CMIP6 models. This further coincides with recent studies showing the precursory nature of NTA SSTs (Ham et al. 2013a, b; Wang et al. 2017; Ma et al. 2020; Sooraj et al. 2023). However, while the selected models show an exaggerated ENSO influence on NTA (in year -1), they also underestimate the possible negative feedback of NTA SSTs on the ENSO transition (in year 0) compared to observations, even in the scenario with higher radiative forcing. This may be a manifestation of complex NTA-ENSO teleconnection biases as inherent in the current state-of-the-art coupled models, which manifest itself as ENSO events persisting far inside year (1) compared to observations in state-of-the art coupled models (Terray et al. 2023). However, this negative feedback seems to strengthen steadily from the historical simulation to the SSP585, thus implying that the feedback of NTA onto ENSO transition is also in line with the strength of the anthropogenic forcing as already suggested from observation in Section 3.

For deeper understanding of this enhanced NTA-ENSO relationship in the future scenarios, in particular the NTA connection to ENSO during year 0, Figure S2 shows box whisker plots illustrating the evolutions across the scenarios for the total number of NTA events [during MAM(0)] and also those preceding the ENSO events [during D(0)JF(1)]. First, a projected increase in the frequency of NTA events is found consistently across the scenarios in all selected 10 models (Fig. S2a), with statistically significant projected increase for the MME10 (see Fig. S2c). The MME10 shows accordingly a relative increase of 18.23%

(20.12%) in ssp245_10m (ssp585_10m) scenarios, as further consistent with the findings presented in Yang et al. (2021). Furthermore, Figure S2b and d demonstrate that, both in the historical and future simulations, many NTA events occurred prior to ENSO events and this behaviour is again better defined in the scenarios, suggesting the key role of NTA SSTs in the future of the biennial ENSO-SASM system. Quantitively for the MME10, the number of NTA events leading to ENSO events is projected to increase approximately by 38% (44%) in ssp245_10m (ssp585_10m), respectively. The results complement those from Yang et al. (2021), using CMIP6 scenarios, showing an increase of NTA events as driven by the previous ENSO state. All together, these results imply that the two-way mutual association between NTA and ENSO is significantly and robustly enhanced in the future global warming scenarios (SSPs).

As illustrated above, the NTA SST anomaly injects a biennial rhythm in the ENSO system and is a key driver of ENSO biennial variability. To pursue this aspect, we performed further analysis to quantify better the future changes in this biennial signature as shown in Figure 7. The biennial signal in NTA-ENSO association is derived based on their mutual associations and is computed as difference in correlation coefficients measuring the ENSO impact on NTA and vice-versa. More precisely, the ENSO impact on NTA (i.e., ENSO_NTA) is calculated as correlation values between Niño3.4 index in D(-1)JF(0) and NTA index in MAM(0), while the NTA impact on ENSO (i.e., NTA_ENSO) is based on the correlation values between NTA index in MAM(0) and Niño3.4 index during D(0)JF(1) for each model. Next, the difference in these correlations is obtained for each model (i.e., ENSO-NTA-ENSO as indicated in the figure caption) and, finally, plotted as an ensemble mean (see Fig. 7a for MME30 and see Fig. 7c for MME10) and is used as a proxy for the amplitude of the biennial cycle in the system as driven by NTA SST anomalies. In observation, both forcings (ENSO to NTA and conversely see Fig. 7a, c) contribute symmetrically to maintain the ENSO biennial variability. However, such symmetric oscillatory behaviour is not well conspicuous in the CMIP6 models (i.e., for its historical simulation): while both the MME30 and MME10 overestimate the ENSO impact on NTA, it shows severe underestimation on the other way around (Fig. 7a, c) consistent with Figure 6. Accordingly, the biennial ENSO signature is underestimated in historical simulations for both the MME10 and MME30, with the selected models (MME10) coming closer to the reality.

It further reveals that the selected 10 models (MME10 compared to MME30) show an enhanced association of NTA MAM(0) SST anomalies to the previous ENSO state [D(-1)JF(0)] with a reduced inter-model spread in both SSPs, thus implying ENSO impacting NTA (i.e., ENSO_NTA) more strongly in the future projections, relative to the historical period (see Fig. 7a, c). Interestingly, this ENSO forcing is not stronger in the highest scenario for both MME10 and MME30, but in the medium scenario. The 10 selected models also exhibit a stronger and more robust negative correlations between MAM(0) NTA and D(0)JF(1) ENSO indices as compared to the 30 models suggesting a steady increase of the negative feedback of NTA to ENSO (i.e., NTA_ENSO) from the historical to the future period, irrespective of the scenario. Moreover, this negative NTA forcing on ENSO increases steadily from the historical simulation to the stronger scenario unlike the reverse ENSO forcing on NTA (ENSO_NTA) for both MME10 and MME30. However, this NTA forcing (i.e., NTA_ENSO) is still much weaker than in current observations, even in the strongest scenario and especially for MME30.

As a consequence of these different changes in the SSPs, the ENSO-NTA-ENSO statistics also increase from the historical simulation to the stronger scenario for both MME30 and MME10, highlighting the key driver role of NTA forcing in this enhanced biennial rhythm of the NTA-ENSO system in the projections irrespective of the strength of the ENSO forcing alone (Fig. 7a, c).

6. Consequence of enhanced NTA-ENSO association on the SASM variability

6.1 Increased SASM variability

In the context of enhanced NTA-ENSO association in the future scenarios as described above, firstly, we analysed the future change in the SD of SASM rainfall. Figure 5b displays box and whisker plots illustrating the SD of SASM rainfall. In the historical period, the SASM rainfall SD ranges from 0.2 to 1.3 mm/day for all the 30 models whereas the selected models show relatively reduced inter-model spread (0.6 to 0.8 mm/day) thus closely resembling the observational estimates (e.g., 0.55 mm/day from GPCP). Recently, Choudhury et al. (2021) and Rajendran et al. (2022) made extensive studies to assess the SASM characteristic in historical simulations of CMIP6 models. According to Rajendran et al. (2022), the SASM variability has systematically improved from previous CMIP generations to CMIP6, as the SASM rainfall SD is underestimated by the previous generations of CMIP models.

Figure 5b further show that the MME10 (MME30) of SASM rainfall SD is 0.75 (0.78), 0.81 (0.85), and 0.88 (0.87) mm/day in hist_10m (historical), ssp245_10m (ssp245), and ssp585_10m (ssp585), respectively. And the future change in rainfall SD with respect to the historical period indicates a percentage increase in the MME10 (MME30) by 8.57% (9%) and

18.07% (11.53%) in ssp245_10m (ssp245) and ssp585_10m (ssp585), respectively. The ensemble mean changes (MME10 and MME30) are further found to be statistically significant (see Figs. 5d, S1d). This increased rainfall variability in the 21st century is further consistent with the findings in Katzenberger et al. (2021).

6.2 Changes in ENSO-SASM teleconnection

As a first step to assess the impact of the enhanced NTA-ENSO association (see previous section) on SASM variability, we examine the lead-lag correlation between the monthly Niño3.4 SST and SASM average rainfall time series for observation and then compared it with historical, SSP245 and SSP585 using selected 10 CMIP6 models (Fig. 6b). The MME10 in both historical and SSPs show two lead-lag correlation peaks of opposite polarity as in observations. Firstly, there is maximum positive correlation in the historical simulation that happens one year before the SASM. The correlations reverse its polarity (positive to negative) during the boreal spring year of 0 and become statistically significant during the JJAS(0) season (e.g., Pandey et al. 2020; Terray et al. 2021; Choudhury et al. 2021). However, both the correlation peaks are much weaker compared to the observation while the correlation values during JJAS of year 0 are much closer to the reality. Furthermore, the peak during year -1 is much broader in observations compared to the simulations, which suggest that the simulation of ENSO transitions is problematic in many models (Terray et al. 2021, 2023). Overall, the simulation of these lead-lag correlations remains a challenge for the current models and the results are much less realistic as compared to the NTA-ENSO lead-lag correlations (e.g., compare Fig. 6a and 6b). In the case of SSP simulations, both the lead and lag correlation peaks are slightly higher in amplitude than in the historical simulation, while the simultaneous correlations during JJAS are almost the same in the historical simulations and the SSPs. This is consistent with the enhanced biennial ENSO anomalies induced by the NTA forcing as documented in the previous section.

Secondly, we obtain the ensemble mean biennial signal in ENSO-SASM system (see Fig. 7b, d), in a similar way as done for the ENSO-NTA system in the previous section, e.g., as difference in correlation coefficients considering the mutual interaction between SASM and ENSO (i.e., ENSO_SASM minus SASM_ENSO, see figure caption for details). The observation shows that the SASM rainfall in JJAS(0) correlate negatively and strongly (-0.5) with the following ENSO during D(0)JF(1), which is in contrast with its counterpart (e.g., ENSO_SASM), thus the former one (SASM_ENSO) contributing dominantly to the biennial statistic of the ENSO-SASM system in observations (i.e., see ENSO_SASM_ENSO statistic in Fig. 7b, d). In the case of CMIP6 models (i.e., for its historical period) both the MME30 and MME10 underestimate the mutual ENSO-SASM interactions (Fig. 7b, d), which is further reflected in the biennial ENSO signature showing underestimation in ENSO-SASM-ENSO statistic as consistent with Figure 6b.

As for the projections, the biennial rhythm in the ENSO-SASM system is greatly enhanced in SSP585 (relative to historical, Fig. 7b, d) for both MME10 and MME30, with an intermediate response in SSP245. Interestingly, the ENSO forcing preceding the SASM (i.e., ENSO_SASM) contributes dominantly to this increased biennial variability of the ENSO-SASM system in the SSPs (see Fig. 7b, d), as the SASM_ENSO statistic stays constant in the historical and SSP simulations despite its greater amplitude (see Fig. 7b, d), while the ENSO_SASM statistic increases steadily in the scenarios as compared to the historical simulation for both MME10 and MME30. This is fully consistent with the driver role of NTA forcing in biennial ENSO variations (Fig. 7a, c) and the emergence of a NTA forcing on SASM as mediated by ENSO in the SSPs.

6.3 Emergence of the NTA forcing in SASM rainfall variability

We further implemented the regression analysis between the NTA PC1 index [MAM(0)] and the SASM rainfall anomalies of the boreal summer season [JJAS(0)] at every grid point over the Indian subcontinent for the future period (2058-2099) in order to get a border perspective on the NTA-SASM teleconnection (see Fig. 3g-h) in the future warming world. The MME10 regressions of SASM rainfall onto the NTA PC1 index from 2058-2099 in the two SSPs show more or less the same anomalous pattern over the Indian subcontinent, but with both SSPs showing more intense and widespread positive rainfall anomalies in the southern Peninsula. The comparison with the historical simulation further illustrates a possible strengthening of the NTA-SASM relationship (Fig. 3g and 3h) in the future warming scenarios, despite that the rainfall anomalies in both the historical and SSP simulations have a reduced amplitude compared to the observations (Fig. 3e-h), which is consistent with the biennial ENSO biases illustrated in Fig. 7a, c.

In order to get a better understanding of the emerging NTA forcing on the changes in SASM variability, we also performed an in-depth composite analysis focussing on NTA-ENSO-SASM associations in the future climate projections based on co-occurring NTA and ENSO events as identified in each selected model (see section 2). These model-based composites are further used to compute the ensemble-average (MME10 mean) across the selected models. More precisely, we constructed two types of NTA-ENSO composites for each model before calculating their MME averages: one for El Niño events preceded by cold-NTA events (referred as CNTA_ElNino) and one for La Niña events preceded by warm-NTA events (referred as WNTA_LaNina). Next, we will describe the results from these two composites, as composite differences (i.e., CNTA_ElNino minus WNTA_LaNina) in both the historical and SSP simulations in order to save place and increase the robustness of the results, leaving the analysis of asymmetric features to another study.

Figure 8 shows the composite differences (as stated above) mean in SST (in panels a, c) and rainfall (in panels b, d) during the boreal spring and summer season [i.e., MAM(0) and JJAS(0)] as computed for the MME10, using the historical simulations. Similar SST and rainfall composite differences are plotted using the SSP245 (see panels e-h) and SSP585 scenarios (see panels i-l). Figure 9a-f depict similar seasonal evolutions for the mean sea level pressure (MSLP) and wind at 850hPa, as done for the composite differences using the historical (see panels a, d), SSP245 (see panels b, e) and SSP585 simulations (see panels c, f). Finally, Figure 9g-i shows composite differences for the velocity potential and divergent wind vector at 850hPa for JJAS(0), using the historical, SSP245 and SSP585 simulations, respectively. Note that the projected future changes (in SSPs as compared to historical) in large-scale features are further tested for statistical significance as shown in Figure S3.

Figure 8a-d depicts robust (e.g. across the selected models) cold SST anomalies over the NTA domain during boreal spring [MAM(0)] with additional SST signature over the north Pacific. As elaborated in recent studies (e.g., Jiang and Li 2019; Park and Li 2019; Terray et al. 2023; Sooraj et al. 2023), the MME10 shows emergence of cold SST anomalies over NTA during the boreal winter of year -1 as often induced by the previous La Niña state (figure not shown). The cold NTA SST anomalies during boreal spring are further significantly enhanced in both future scenarios and found to persist even during boreal summer for SSP585 (see Figs. 8e-l and see S3a-h for significance in future changes). Both in historical (Fig. 8a-d) and future simulations (Fig. 8e-l), the boreal spring cold NTA SST anomalies are further accompanied by significantly suppressed rainfall over the tropical Atlantic north of the Equator indicating a southward shift of the Intertropical Tropical Convergent Zone (ITCZ) which assumes significantly stronger values in the future simulations, see Figs. 8 e-l and S3a-h. Interestingly, the MME10 for the historical period clearly depicted the observed dipole rainfall structure with suppressed (enhanced) rainfall anomalies north (south) of the equator during boreal spring, as described in Sooraj et al. (2023), with the future simulations (in particular SSP585) showing the increased magnitude of future response. In fact, this meridional dipole rainfall structure in boreal spring is more prominent and distinct in future simulations than in historical simulations. There is an associated anomalous anticyclonic circulation over the NTA region (during boreal spring, see Fig. 9) in the form of northeasterly winds emanating from the Azores high, thus triggering cold NTA anomalies through wind–evaporation–SST feedback (WES; e.g., Amaya et al. 2017; Yang et al. 2018). These coupled evolutions of SST, rainfall and circulation anomalies over the Tropics and the with strengthening of their signatures in the future simulations suggest a more active WES feedback (Yang et al. 2021; Sooraj et al. 2023) in the future climate. In agreement with this hypothesis, Yang et al. (2021), while analysing the NTA variability in CMIP6 future projections inferred that the modulation of Atlantic trade winds may further strengthen the local ocean-atmosphere coupling in a future warming climate through changes in oceanic mixed layer depth.

Next, there are distinct extra-tropical circulation features (in the form of wave trains extending to mid-latitudes) over the North Pacific suggesting also ENSO teleconnections in all simulations. Furthermore, these anomalous circulation features show consistent strengthening in the projections (see Fig. 9a-f) and, as shown by recent studies, they play vital roles in the ENSO transitions through two pathways (e.g., Terray et al. 2023; Sooraj et al. 2023). Firstly, the anomalous extra-tropical circulation over the North Pacific may create El Niño favouring southerly/southwesterly wind anomalies over the subtropical North Pacific during MAM(0) to JJAS(0) period playing both an important local role in ENSO transition and remotely forcing the NTA (e.g., Boschat et al. 2013; Jiang and Li 2019). Secondly, the suppressed convection over NTA generates an anomalous east–west overturning circulation (see Fig. 9g-i), thus promoting westerlies over the western Pacific which in-turn further contributes to the El Niño warming conditions (Jiang and Li 2019, 2021; Sooraj et al. 2023).

For the boreal summer period during JJAS(0), the composite differences (CNTA_ElNino minus WNTA_LaNina composites) show large-scale dryness over the Indian subcontinent (Fig. 8b,d,f,h,j,l) extending to Bay of Bengal and maritime continent in both the historical and future simulations. Consistent with Fig. 3f-h, these negative rainfall anomalies are amplified in future simulations, especially in SSP585 (Fig. S3h). Further, the rainfall anomalies averaged over the Indian land region (10°N to 30°N and 70°E to 95°E) in the MME10 composite differences show values of -5.6 mm/day, -6.3 mm/day, and -6.41 mm/day for historical, SSP245, and SSP585, respectively. In terms of percentage future rainfall change with respect to the historical period, it indicates an increase of 12.5% and 14.5%, in SSP245 and SSP585, respectively. The composites also show an anomalous increase in the MSLP to the west of the India with a consistent weakening of the continental monsoon trough which further coincides with anomalously weakened low-level westerlies (Fig. 9d-f). Further corroborating this weakening large-scale signal, there is strengthened low-level divergence (convergence) over the Indian region (tropical Pacific) in the SSP245 and SSP585 scenarios (Fig. 9g-i).

All these results illustrate a significant modification in low-level monsoon flow and in the associated large-scale rainfall signatures in future scenarios, thus confirming noticeable changes in the NTA-ENSO-SASM teleconnection in the future climate, partly induced by an enhanced NTA forcing on the ENSO-SASM system as demonstrated in the previous sections. In the next section, we investigate if the emergence of this NTA forcing is related to specific SST mean-state changes, especially an enhanced warming of the NTA relative to the Tropics in the two scenarios.

7. Possible origin of stronger biennial variability in NTA-ENSO-SASM system in the future projections

Figure 10a-b further explores the origin of the enhanced biennial signatures of the NTA-ENSO-SASM system in the scenarios by conducting inter-model correlation analysis between the future SST mean-state changes and the future change in biennial signatures in ENSO-NTA (i.e., recall the ENSO-NTA-ENSO static as used in Fig. 7a, c), using all 30 CMIP6 models. Note that for the future SST changes, we have removed the averaged mean over the tropics (30°S to 30°N) at every grid point in each model before performing the correlation analysis across the 30 CMIP6 models. For further ease in interpretations, we conducted similar analysis but replacing the biennial signatures with the interannual variability (SD) in ENSO (Fig. 10c-d) and SASM (Fig. 10e-f).

Figure 10a-b basically shows the existence of strong and significant linear relationship between the future change in biennial signature for the ENSO-NTA system (i.e., ENSO-NTA-ENSO static) and the future SST change over the Tropics. There are significant correlation signatures extending from North-eastern Pacific to equatorial Pacific with additional signatures over NTA and North-western Pacific. In the equatorial Pacific, there is a clear and consistent weakening of the equatorial SST gradient in both scenarios, but this modulation is not stronger in the SSP585 scenario. Importantly, this highest emission scenario also shows a well-defined interhemispheric differential warming pattern, which is much less obvious in SSP245. These different mean-state changes are also linearly associated with an enhanced ENSO variability across the models, as further reflected in Figure 10c-d, thus exemplifying the prominent common drivers for enhancing the ENSO variability and the biennial signature in the NTA-ENSO system under global warming scenarios. First, the reduced Pacific equatorial SST gradient in the future scenarios means that the eastern equatorial Pacific warms faster than the west Pacific, which is usually associated with reduced upwelling in the eastern Pacific and a flattened thermocline in the equatorial Pacific and it has been suggested that these mean state changes may enhance ENSO variability. As an illustration, Zheng et al. (2016) suggested that such modulation of the Pacific equatorial SST gradient is a major source of ENSO amplitude changes in the coupled models as the ENSO amplitude may increase when the barrier to deep convection is reduced in the eastern equatorial Pacific. Obviously, such Pacific equatorial mean state changes may also be an important driver of the enhanced biennial signature of the ENSO-NTA system (Fig. 10a, b) as this may result in an enhanced ENSO-NTA teleconnections in the projections (Fig. 7a, c). Importantly, beside the role of the Pacific equatorial SST gradient, Figure 10a-d highlight the potential role of NTA relative warming in enhancing both the ENSO variability and the biennial variations of the NTA-ENSO system, which is consistent with its emerging role in the recent observed period as documented in Section 3. If we interpret this relative NTA SST warming as a proxy for convective instability, this may suggest that NTA events may exert a larger forcing outside the NTA region, especially in the Eastern Pacific and remote regions as India.

Earlier studies have indicated that the boreal winter-to-spring SST anomalies over the Indian Ocean (i.e., Indian Ocean Basin-wide, IOB mode) can also influence the ENSO events and also contributes greatly to its biennial rhythm in observations as NTA (e.g., Meehl et al. 2003; Xie et al. 2009; Terray et al. 2016; Yang et al. 2023). Intriguingly, in both Figure 10a-b and 10c-d, there is no warming or cooling signature over the Indian Ocean thus ruling out the role of Indian Ocean and its relative mean-state warming as a driver of ENSO amplitude changes or even for modulating the ENSO biennial rhythm in the future climate projections. This is in strike contrast to the significant role of the NTA relative warming in both ENSO variability and the NTA-ENSO system shown in Figure 10a-d. However, the SST mean-state changes of the tropical Indian Ocean emerge as a major source of amplitude SASM rainfall changes, which may be understood as the Indian Ocean is the major source of water vapor to feed the Indian monsoon (e.g., Levine and Turner 2012; Ratna et al. 2016), while both the modulation of the equatorial Pacific SST gradient and the relative NTA warming seem to play minor roles on SASM rainfall amplitude changes in sharp contrast to ENSO variability (Fig. 10e-f).

Thus, both the modulation of the Pacific equatorial SST gradient and the NTA relative warming play an important role in contributing to the ENSO variability and its biennial characteristics under future projections (in both SSPs, see Fig. 10a-d), which may further change the characteristics of the ENSO-SASM teleconnections (Fig. 7), but this is not sufficient by itself to emerge as main drivers of SASM variability changes across the scenarios, which is also governed by other factors such as the Indian Ocean variability or the zonal SST contrast in the Indo-Pacific ocean (e.g., Chen 2003).

8. Discussion and Summary

The NTA SST mode during boreal spring plays an important role in influencing ENSO and its biennial time scale according to the recent observational and modeling studies (Ham et al. 2013a, b; Wang et al. 2017; Sooraj et al. 2023). This recent growing recognition of NTA SSTs in the ENSO transitions brings the former one to the fore as an emerging driver of the ENSO-SASM system through a positive mutual association between ENSO, SASM rainfall and pre-monsoon NTA SST anomalies as distinctly demonstrated in model sensitivity experiments (Terray et al. 2023; Sooraj et al. 2023). Observational evidence further suggests a strengthening of the relationship between SASM rainfall and the NTA SST in recent decades due to an increased NTA-ENSO association (Fig. 2a). Moreover, the future climate projections from CMIP6 indicate an increase in NTA SST and SASM rainfall variabilities (Yang et al. 2021; Douville et al. 2021; Katzenberger et al. 2021), while it shows a significant weakening of the AZM-SASM association in future warming projections (Sabeerali et al. 2022). In the backdrop of these results, the current study attempted to bring more clarity on whether the ENSO-SASM association as mediated through NTA SSTs undergoes significant modulations in the future warming climate.

Firstly, we analyzed the fidelity of the current state-of-the-art coupled models to capture the present-day climatology and variability aspects of the NTA-SASM system using 30 CMIP6 models. Only 10 CMIP6 models (out of 30) adequately captured statistics of the NTA-SASM system in the historical simulation, though all the 30 models realistically simulated the ENSO variability statistics. Therefore, we used mainly these 10 CMIP6 models to study the NTA-

ENSO-SASM teleconnection in future simulations (SSP245and SSP585), but some of the important results are also checked using all the 30 models.

All the 30 CMIP6 models (and in particular the 10 selected models) show significant enhanced NTA and ENSO variabilities under greenhouse induced global warming scenarios, especially for NTA (see Figs. 4b, d, 5a, c). Interestingly, the increased NTA variability in both SSPs (both in 30 and selected 10 models) shows also a better inter-model agreement, in contrast to the larger inter-model spread for the change in Niño3.4 variability, as consistent with Fredriksen et al. (2020). But on the other hand, it is also encouraging to note that there is a reduced inter-model spread in the selected models (relative to the 30 models see Figs. 4b, d, 5a, c) for both the ENSO and NTA variability thus emphasising the importance to carefully evaluate the CMIP6 models' skill in realistically representing the observed ENSO and NTA variability (Fredriksen et al. 2020). This further justifies our selection of models thus enabling us to observationally constrain the future projected changes of ENSO and NTA variability.

Consistent with recent observations, our results further show a strengthening of the NTA-ENSO teleconnection in both future scenarios with enhanced NTA forcing onto ENSO in future projections (see Figs. 6a, 7a, c). In consonance with this emerging NTA signature, there is future strengthening of the biennial signature as associated with the NTA-ENSO and ENSO-SASM teleconnections (see Fig. 7). Note that this is in sharp contrast to the projected significant weakening of the AZM-SASM as noted recently (Sabeerali et al. 2022). This brings up the significance of NTA relative warming to account for the future strengthening of the biennial signature in ENSO variability (see Fig. 10a-d), with the zonal SST gradients in the equatorial Pacific playing an additional role. Interestingly, the future increase in SASM rainfall variability and its enhanced biennial signature are not distinctively driven by these factors (Fig. 10 e, f), which partially coincides with the known fact that the SASM rainfall variability is also governed by the moisture variability over the Indian Ocean (e.g., Levine and Turner 2012; Ratna et al. 2016).

In contrast with the projected enhancements in biennial signature of ENSO-SASM teleconnection, our results show only a modest strengthening of the ENSO-SASM relationships in the future warming scenarios (in both SSPs, see Fig. 6b). Earlier studies have also hypothesized either weakening or strengthening of the ENSO-SASM relationship in the future climate projections under CMIP5 and CMIP6 (Li and Ting 2015; Azad and Rajeevan 2016; Roy et al. 2019; Lee and Bodoi 2021; Goswami and An 2023). For example, a recent study using CMIP6 future projections show no robust change in ENSO-SASM relationship during the 21st century, while their results based on the large-ensemble archives from MPI-ESM reveal significant strengthening of the ENSO-SASM relationship in response to GHG forcing (Lee and Bodoi 2021). This is further contrasted with a weakening of the ENSO-SASM teleconnection in idealized climate warming simulations (Goswami and An 2023). These contradictory results on the future changes in ENSO-SASM relationship probably suggest that the SASM variability is not uniquely driven by ENSO, which further coincides with our results. Interpreted differently, this stresses the need to take into account the role of Indian Ocean variability for the future projection of SASM variability and, by extension, all the tropical inter-basin interactions for assessing the future changes of the ENSO-SASM system under a warming world (Cai et al. 2019). In line of this argument, recently Yang et al. (2023) has showed the synergistic effect of the IOB (Xie et al. 2009) and NTA events on the ENSO transitions. We already started investigating this aspect using CMIP6 projections and the results will be documented in an accompanying study.

An aspect which must also deserve greater attention from the scientific community is the prominent teleconnection biases in the current state-of-the-art coupled models as manifested with reduced negative feedback (as compared to the observed feedback) of Atlantic and Indian oceans onto ENSO in the current models (see Terray et al. 2021, 2023). The results from this study are consistent with this assertion (see Figs. 6a, 7a, c) as they illustrate a severe underestimation of the NTA impact on ENSO transitions (in year 0) in the historical period. This has implications in our confidence of future changes of the whole ENSO-SASM system based on CMIP6 models, as the feedback of NTA onto ENSO transition is probably severely underestimated in the projections as well (see Fig. 7a, c).

It is well known that state-of-the-art coupled models suffer from persistent and systematic errors, in particular over the tropical Atlantic (Wang et al. 2014; Cabos et al. 2019). Furthermore, these biases have large implications in truly representing the mutual NTA-ENSO associations (e.g., Cai et al. 2019; Cabos et al. 2019), thus in-turn impacting the ENSO variability characteristics both in the historical and future projections. The specific role of the coupled model biases on future projections is beyond the scope of this study, but needs to be explored as it can modulate the future changes in the NTA-ENSO-SASM teleconnections and its associated biennial variabilities as simulated by climate models, thus leading to uncertainties and a large inter-model spread in the climate projections. Our future works will be focused in this direction.

Acknowledgments

We sincerely thank Dr. R. Krishnan, Director, Indian Institute of Tropical Meteorology (IITM, India) and Dr. J. Sanjay, Project Director, Centre for Climate Change Research (CCCR at IITM) for all the support during the research study. Ajinkya M. Aswale, Sooraj K P and Swapna P are funded by the CCCR and IITM, which are fully funded by the Ministry of Earth Sciences, Government of India. Pascal Terray is funded by Institut de Recherche pour le Développement (IRD, France). This work is a part of the Ph.D. Thesis of the first author.

Funding

The authors have no funding reference to declare.

Data Availability

All the observational datasets used in this study are publicly available, and the CMIP6 model datasets used for this study are available through the ESGF repository https://esgf-node.llnl.gov/search/cmip6/. The analysis was carried out utilizing open-source software tools such as the Climate Data Operators and Python (https://www.python.org/) for the computations and visualizations.

Conflict of interest

The authors have not disclosed any competing interests.

Author Contributions

Ajinkya M Aswale (AMA) conducted the analysis, formulated methodology, handled software and visualization tools, analysed the results, and wrote the original manuscript. SKP (Sooraj K P), SP (Swapna Panickal) and TP (Terray Pascal) wrote the original draft, reviewed and edited the manuscript.

References

Adler RF, Sapiano MRP, Huffman GJ, et al (2018) The Global Precipitation Climatology Project (GPCP) monthly analysis (new version 2.3) and a review of 2017 global precipitation. Atmosphere (Basel) 9:138

Amaya DJ, DeFlorio MJ, Miller AJ, Xie S-P (2017) WES feedback and the Atlantic meridional mode: Observations and CMIP5 comparisons. Clim Dyn 49:1665–1679

Azad S, Rajeevan M (2016) Possible shift in the ENSO-Indian monsoon rainfall relationship under future global warming. Sci Rep 6:20145

Boschat G, Terray P, Masson S (2013) Extratropical forcing of ENSO. Geophysical Research Letters, 40(8), 1605-1611.

Cabos W, de la Vara A, Koseki S (2019) Tropical Atlantic variability: observations and modeling. Atmosphere 10:502. https://doi.org/10.3390/atmos10090502

Cai W, Santoso A, Collins M, et al (2021) Changing El Niño–Southern oscillation in a warming climate. Nat Rev Earth Environ 2:628–644

Cai W, Wang G, Dewitte B, et al (2018) Increased variability of eastern Pacific El Niño under greenhouse warming. Nature 564:201–206

Cai W, Wu L, Lengaigne M, et al (2019) Pantropical climate interactions. Science (1979) 363:6430. https://doi.org/10.1126/science.aav4236

Chattopadhyay R, Phani R, Sabeerali CT, et al (2015) Influence of extratropical sea□surface temperature on the Indian summer monsoon: an unexplored source of seasonal predictability. Quarterly Journal of the Royal Meteorological Society 141:2760–2775

Chen TC (2003) Maintenance of summer monsoon circulations: a planetary-scale perspective. J Climate 16:2022–2037

Chen Z, Zhou T,Zhang L, Chen X, et al (2020) Global land monsoon precipitation changes in CMIP6 projections. Geophys. Res. Lett., 47, e2019GL086902, https://doi.org/10.1029/2019GL086902

Chiang JCH, Vimont DJ (2004) Analogous Pacific and Atlantic meridional modes of tropical atmosphere–ocean variability. J Clim 17:4143–4158

Choudhury BA, Rajesh P V, Zahan Y, Goswami BN (2021) Evolution of the Indian summer monsoon rainfall simulations from CMIP3 to CMIP6 models. Clim Dyn 1–26

Ding H, Keenlyside NS, Latif M (2012) Impact of the Equatorial Atlantic on the El Niño Southern Oscillation. Clim Dyn 38:1965–1972. https://doi.org/10.1007/s00382-011-1097-y

Douville H, Raghavan K, Renwick J, et al (2021) Water cycle changes, Chap 8. Intergovernmental panel for climate change (IPCC), Working group 1 (WG1), Sixth assessment report (AR6)

Eyring V, Bony S, Meehl GA, et al (2016) Overview of the Coupled Model Intercomparison Project Phase 6 (CMIP6) experimental design and organization. Geosci Model Dev 9:1937–1958

Fredriksen H, Berner J, Subramanian AC, Capotondi A (2020) How does El Niño–Southern Oscillation change under global warming—A first look at CMIP6. Geophys Res Lett 47:e2020GL090640

Goswami BB, An SI (2023) An assessment of the ENSO-monsoon teleconnection in a warming climate. npj Clim Atmos Sci 6, 82. https://doi.org/10.1038/s41612-023-00411-5

Guilbert M, Terray P, Mignot J (2023) Intermodel Spread of Historical Indian Monsoon Rainfall Change in CMIP6: The Role of the Tropical Pacific Mean State. J Clim 36:3937–3953

Ham Y-G, Kug J-S, Park J-Y, Jin F-F (2013a) Sea surface temperature in the north tropical Atlantic as a trigger for El Niño/Southern Oscillation events. Nat Geosci 6:112–116

Ham Y, Kug J, Park J (2013b) Two distinct roles of Atlantic SSTs in ENSO variability: North tropical Atlantic SST and Atlantic Niño. Geophys Res Lett 40:4012–4017

Jiang L, Li T (2019) Relative roles of El Niño-induced extratropical and tropical forcing in generating Tropical North Atlantic (TNA) SST anomaly. Clim Dyn 53:3791–3804. https://doi.org/10.1007/s00382-019-04748-7

Katzenberger A, Schewe J, Pongratz J, Levermann A (2021) Robust increase of Indian monsoon rainfall and its variability under future warming in CMIP6 models. Earth System Dynamics 12:367–386

Kitoh A, Endo H, Krishna Kumar K, et al (2013) Monsoons in a changing world: A regional perspective in a global context. Journal of Geophysical Research: Atmospheres 118:3053–3065

Kucharski F, Bracco A, Yoo JH, et al (2009) A Gill-Matsuno-type mechanism explains the tropical Atlantic influence on African and Indian monsoon rainfall. Quarterly Journal of the Royal Meteorological Society 135:569–579. https://doi.org/10.1002/qj.406

Lee J-Y, Bódai T (2021) Future changes of the ENSO–Indian summer monsoon teleconnection. In: Indian Summer Monsoon Variability. Elsevier, pp 393–412

Levine RC, Turner AG (2012). Dependence of Indian monsoon rainfall on moisture fluxes across the Arabian Sea and the impact of coupled model sea surface temperature biases. Climate Dynamics, 38, 2167-2190.

Li X, Ting M (2015) Recent and future changes in the Asian monsoon□ENSO relationship: Natural or forced? Geophys Res Lett 42:3502–3512

Ma J, He W, Chen Z, et al (2020) The impact of north tropical Atlantic sea surface temperature anomalies in the ensuing spring of El Niño on the tropical Indian Ocean and Northwest Pacific. International Journal of Climatology 40:4978–4991

Meehl GA, Arblaster JM, Loschnigg J (2003) Coupled ocean–atmosphere dynamical processes in the tropical Indian and Pacific Oceans and the TBO. Journal of Climate, 16(13), 2138-2158.

Noreen EW (1989) Computer-intensive methods for testing hypotheses: an introduction. John Wiley & Sons, New York

O'Neill BC, Tebaldi C, Van Vuuren DP, et al (2016) The scenario model intercomparison project (ScenarioMIP) for CMIP6. Geosci Model Dev 9:3461–3482

Pai DS, Rajeevan M, Sreejith OP, et al (2014) Development of a new high spatial resolution (0.25× 0.25) long period (1901-2010) daily gridded rainfall data set over India and its comparison with existing data sets over the region. Mausam 65:1–18

Pandey P, Dwivedi S, Goswami BN, Kucharski F (2020) A new perspective on ENSO-Indian summer monsoon rainfall relationship in a warming environment. Clim Dyn 55:3307–3326

Park J-H, Kug J-S, Yang Y-M, et al (2022) Role of the climatological North Pacific High in the North Tropical Atlantic–ENSO connection. J Clim 35:6815–6826

Park J-H, Li T (2019) Interdecadal modulation of El Niño–tropical North Atlantic teleconnection by the Atlantic multi-decadal oscillation. Clim Dyn 52:5345–5360. https://doi.org/10.1007/s00382-018-4452-4

Park J-H, Yeh S-W, Kug J-S, et al (2023) Two regimes of inter-basin interactions between the Atlantic and Pacific Oceans on interannual timescales. NPJ Clim Atmos Sci 6:13 https://doi.org/10.1038/s41612-023-00332-3

Parthasarathy B, Munot AA, Kothawale DR (1994) All-India monthly and seasonal rainfall series: 1871–1993. Theor Appl Climatol 49:217–224

Rajeevan M, Sridhar L (2008) Inter□annual relationship between Atlantic sea surface temperature anomalies and Indian summer monsoon. Geophys Res Lett 35: L21704. doi:10.1029/2008GL036025

Rajendran K, Surendran S, Varghese SJ, Sathyanath A (2022) Simulation of Indian summer monsoon rainfall, interannual variability and teleconnections: evaluation of CMIP6 models. Clim Dyn 58:2693–2723

Rayner NA, Parker DE, Horton EB, Folland CK, Alexander LV, Rowell DP, Kent EC, Kaplan A (2003) Global analyses of sea surface temperature, sea ice, and night marine air temperature since the late nineteenth century. J Geophys Res 108(D14):4407. https://doi.org/10.1029/2002JD002670

Ratna SB, Cherchi A, Joseph PV, et al (2016). Moisture variability over the Indo-Pacific region and its influence on the Indian summer monsoon rainfall. Climate dynamics, 46, 949-965. DOI 10.1007/s00382-015-2624-z.

Roy I, Gagnon AS, Siingh D (2019) Evaluating ENSO teleconnections using observations and CMIP5 models. Theor Appl Climatol 136:1085–1098

Sabeerali CT, Ajayamohan RS, Bangalath HK, Chen N (2019) Atlantic Zonal Mode: An Emerging Source of Indian Summer Monsoon Variability in a Warming World. Geophys Res Lett 46:4460–4467. https://doi.org/10.1029/2019GL082379

Sabeerali CT, Ajayamohan RS, Praveen V (2022) Atlantic zonal mode-monsoon teleconnection in a warming scenario. Clim Dyn 58:1829–1843. https://doi.org/10.1007/s00382-021-05996-2

Saji NH, Goswami BN, Vinayachandran PN, Yamagata T (1999) A dipole mode in the tropical Indian Ocean. Nature 401:360–363

Sharmila S, Joseph S, Sahai AK, et al (2015) Future projection of Indian summer monsoon variability under climate change scenario: An assessment from CMIP5 climate models. Glob Planet Change 124:62–78

Sooraj KP, Aswale AM, Swapna P, et al (2023) Modulations in the Indian Summer Monsoon–ENSO teleconnections by the North Tropical Atlantic. Clim Dyn 1–20

Sooraj KP, Terray P, Mujumdar M (2015) Global warming and the weakening of the Asian summer monsoon circulation: assessments from the CMIP5 models. Clim Dyn 45:233–252

Taylor KE (2001) Summarizing multiple aspects of model performance in a single diagram. Journal of geophysical research: atmospheres 106:7183–7192

Terray P, Delécluse P, Labattu S, Terray L (2003). Sea surface temperature associations with the late Indian summer monsoon. Climate Dynamics, 21, 593-618.

Terray P, Masson S, Prodhomme C, et al (2016) Impacts of Indian and Atlantic oceans on ENSO in a comprehensive modeling framework. Clim. Dyn. 46, 2507-2533 doi: 10.1007/s00382-015-2715-x

Terray P, Joseph L, Sooraj KP (2023) Anatomy of the Indian summer monsoon and ENSO relationship in a state-of-the-art CGCM: role of the tropical Atlantic Ocean. Clim Dyn 60:1559–1582

Terray P, Sooraj KP, Masson S, Prodhomme C (2021) Anatomy of the Indian Summer Monsoon and ENSO relationships in state-of-the-art CGCMs: Role of the tropical Indian Ocean. Clim Dyn 56:329–356

Wang C, Kucharski F, Barimalala R, Bracco A (2009) Teleconnections of the tropical atlantic to the tropical Indian and Pacifc oceans: a review of recent fndings. Meteorol Zeitschrift 18(4):445–454. https://doi.org/10.1127/0941-2948/2009/0394

Wang L, Yu JY, Paek H (2017) Enhanced biennial variability in the Pacific due to Atlantic capacitor effect. Nat Commun. https://doi.org/10.1038/ncomms14887

Wang C, Zhang L, Lee SK, et al (2014) A global perspective on CMIP5 climate model biases. Nat Clim Change 4:201–205

Webster PJ, Magana VO, Palmer TN, et al (1998) Monsoons: Processes, predictability, and the prospects for prediction. J Geophys Res Oceans 103:14451–14510

Xie SP, Hu K, Hafner J, et al (2009) Indian Ocean capacitor effect on Indo–western Pacific climate during the summer following El Niño. *Journal of climate*, *22*(3), 730-747.

Yang X, Huang P (2021) Restored relationship between ENSO and Indian summer monsoon rainfall around 1999/2000. The Innovation 2:100102. https://doi.org/10.1016/j.xinn.2021.100102

Yang Y, Wu L, Guo Y, et al (2021) Greenhouse warming intensifies north tropical Atlantic climate variability. Sci Adv 7:eabg9690

Yang Y, Xie SP, Wu L, et al (2018) ENSO forced and local variability of North Tropical Atlantic SST: model simulations and biases. Clim Dyn 51:4511–4524. https://doi.org/10.1007/s00382-017-3679-9

Yang G, Zhao X, Yuan D, et al (2023). Synergistic Effect of Warming in the Tropical Indian Ocean and North Tropical Atlantic on the Central-Pacific Type of La Nina Based on Observations and CMIP5. Journal of Climate, 36(24), 8561-8579.

Zheng XT, Xie SP, Lv LH, Zhou ZQ (2016) Intermodel uncertainty in ENSO amplitude change tied to Pacific Ocean warming pattern. J. Climate, 29, 7265-7279

Figures:

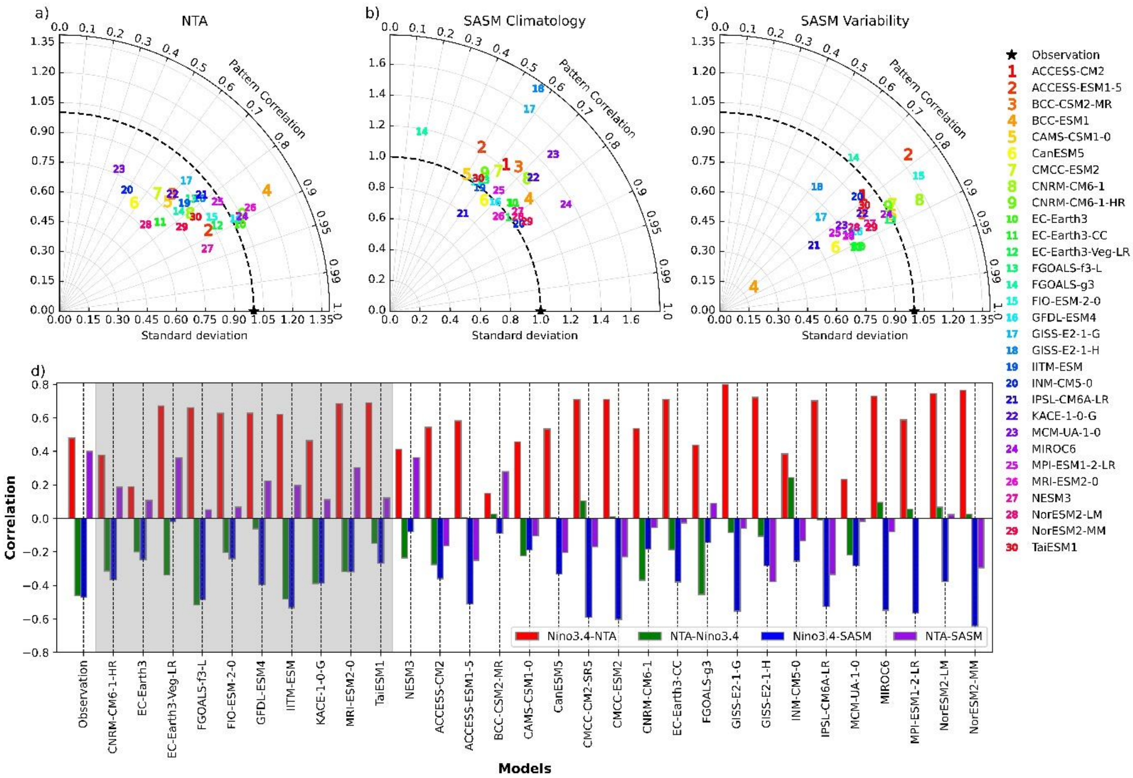

Fig. 1: (a) Taylor diagram showing the skill of 30 CMIP6 Models in reproducing the spatial pattern of EOF1 of NTA SSTA, for MAM season (see Section 2 for more details). In (b), same as a), but for the JJAS climatology of rainfall over Indian landmass (i.e., South Asian Summer Monsoon, SASM region over 10°N to 30°N and 70°E to 95°E). In (c), same as a), but for the interannual variability of rainfall over Indian Landmass during JJAS period. In (d), correlation between various indices as done for the historical period: Niño3.4 during D(-1)JF(0) and NTA during MAM(0) [red bars], NTA during MAM(0) and Niño3.4 during D(0)JF(1) [green bars], SASM during JJAS(0) and Niño3.4 during JJAS(0) [blue bars], NTA during MAM(0) and SASM during JJAS(0) [purple bar]. The selected models are highlighted in gray color. See Section 2 for more details on NTA, Niño3.4 and SASM indices. The observed analysis used GPCP and HadISST datasets.

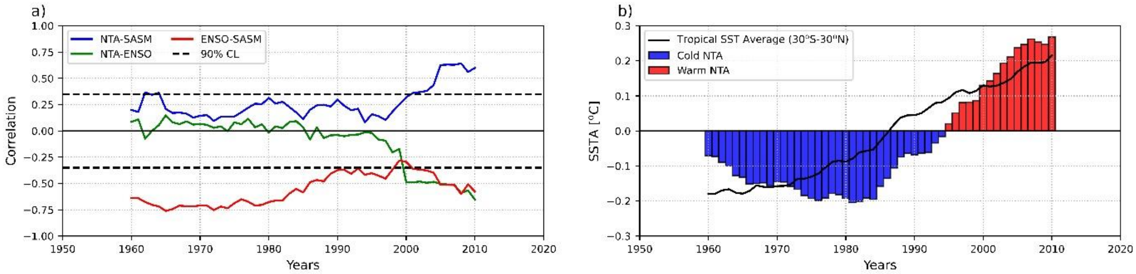

Fig. 2: In (a), 21-year running correlation between various indices during the observed period 1948–2020. The sliding correlation between SASM rainfall index (for JJAS season) and NTA PC1 index (for MAM) is shown in blue line, while the correlation between NTA PC1 index and ENSO SST index during JJAS is in green line. Similar sliding correlation between ENSO SST index and SASM rainfall is shown in red line. In (b), 21-year running average of NTA SST anomalies averaged over the region 0° to 30°N and 70°W to 10°W (blue and red bars) and Tropical Ocean SST anomalies as averaged over 30°S to 30°N and 180°W to 180°E (solid black line). See section 2 for the definitions of the NTA, ENSO (Niño3.4) and SASM indices. Here we used the observed data for the period from 1948 to 2020 in order to depict the long-term changes in NTA-ENSO-SASM association. Accordingly, in (a), we used IMD dataset as GPCP is available from 1979 onwards. Importantly, note that the anomalies in Fig. 2b are not detrended unlike in rest of the figures. The 90% confidence level (CL) based on the bootstrap test is marked in (a).

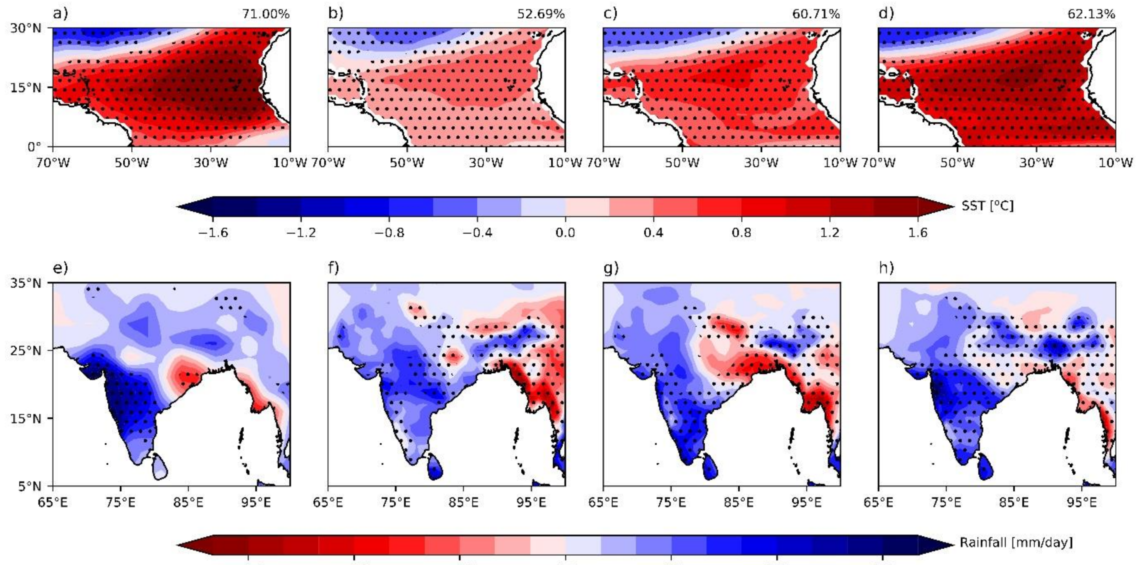

Fig. 3: In (a), spatial regression between the NTA PC1 index and the boreal spring (MAM) SST anomalies over the NTA region, using observation (HadISST). In (b), (c) and (d), same as (a), but based on ensemble mean (MME10) using historical, SSP245 and SSP585 scenarios. In (e), spatial regression of JJAS rainfall anomalies onto NTA PC1 index for observation (GPCP). In (f), (g) and (h), same as (e), but for the MME10 using historical, SSP245 and SSP585 scenarios. Note that for both historical and SSPs, the spatial regressions are computed for each selected model and the ensemble mean (MME10) is finally shown. The stippling in figures (a) and (e) indicate that the SST and rainfall anomalies are significant above 90% confidence level following the bootstrap method, while the stippling in figures (b) to (d) and (f) to (h) indicates that the multi-model mean is greater than or equal to 1 Standard Deviation (SD).

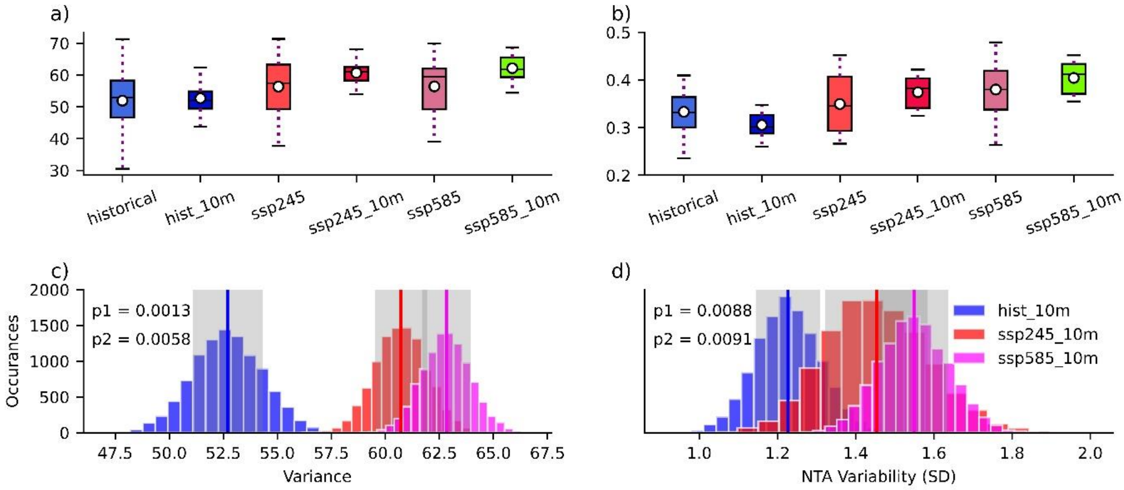

Fig. 4: In a) Box and whisker plots illustrating the NTA variance (%) explained by the first mode of EOF analysis applied to the boreal spring (for MAM season) SST anomalies over the NTA domain using historical, SSP245 and SSP585 scenarios. In (b), same as (a) but for the NTA SST variability (SD, °C). In (a) and (b), the statistics are computed for all the 30 (refer to historical, ssp245 and ssp585) and selected 10 (refer to hist_10m, ssp245_10m and ssp585_10m) CMIP6 models. The whiskers outside the box represent the total inter-model range, while the boxes indicate the interquartile model spread with the median represented by the line inside the box. The MME of 10 selected and 30 CMIP6 models (referred in the main text as MME10 and MME30, respectively) is shown by white circles with a black border. In (c), the histograms of 10,000 realizations of the bootstrap method for NTA EOF variance using the historical (for the period 1973 to 2014, blue), SSP245 (for the period 2058 to 2099, red) and SSP585 (for the period 2058 to 2099, magenta) scenarios, as done with selected 10 CMIP6 models. In (d), same as (c), but for NTA SST SD. In (c-d), the blue lines indicate the mean value of the 10,000 realizations as computed for the historical period. The red (magenta) lines represent the similar means as computed using SSP245 (SSP585) scenarios, for the future period. The gray coloured regions correspond to 1 SD of the 10,000 realizations. The p-values (p1 is for ssp585_10m and p2 is for ssp245_10m) based on bootstrap tests are indicated (Noreen 1989; Terray et al. 2003, see Section 2 for details).

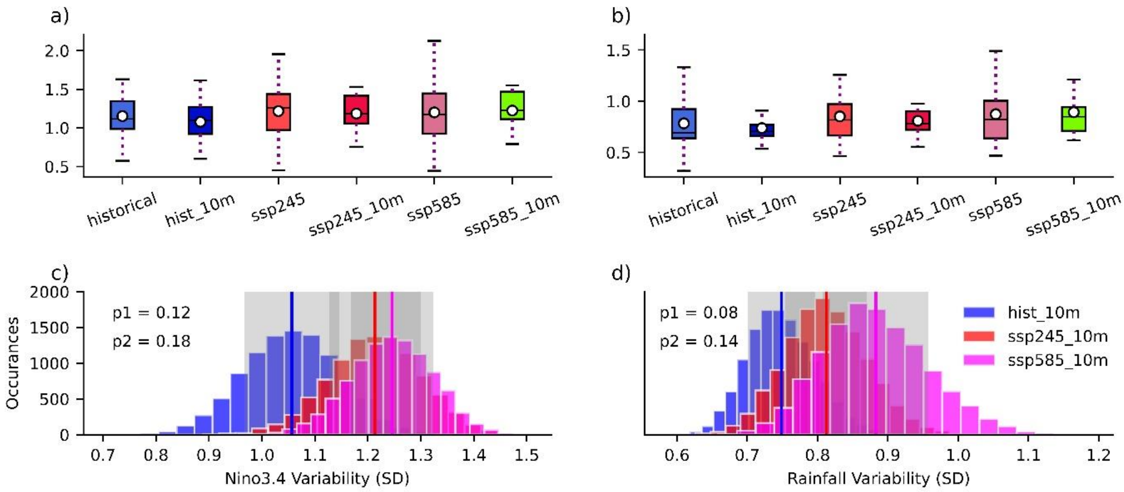

Fig. 5: In (a) and (c), same as Figures 4a and 4c, but for box and whisker plots illustrating the Niño3.4 variability (SD, °C) during boreal winter (December to February). In (b) and (d), same as Figures 4b and 4d, but for the SASM rainfall SD (mm/day) during the JJAS period.

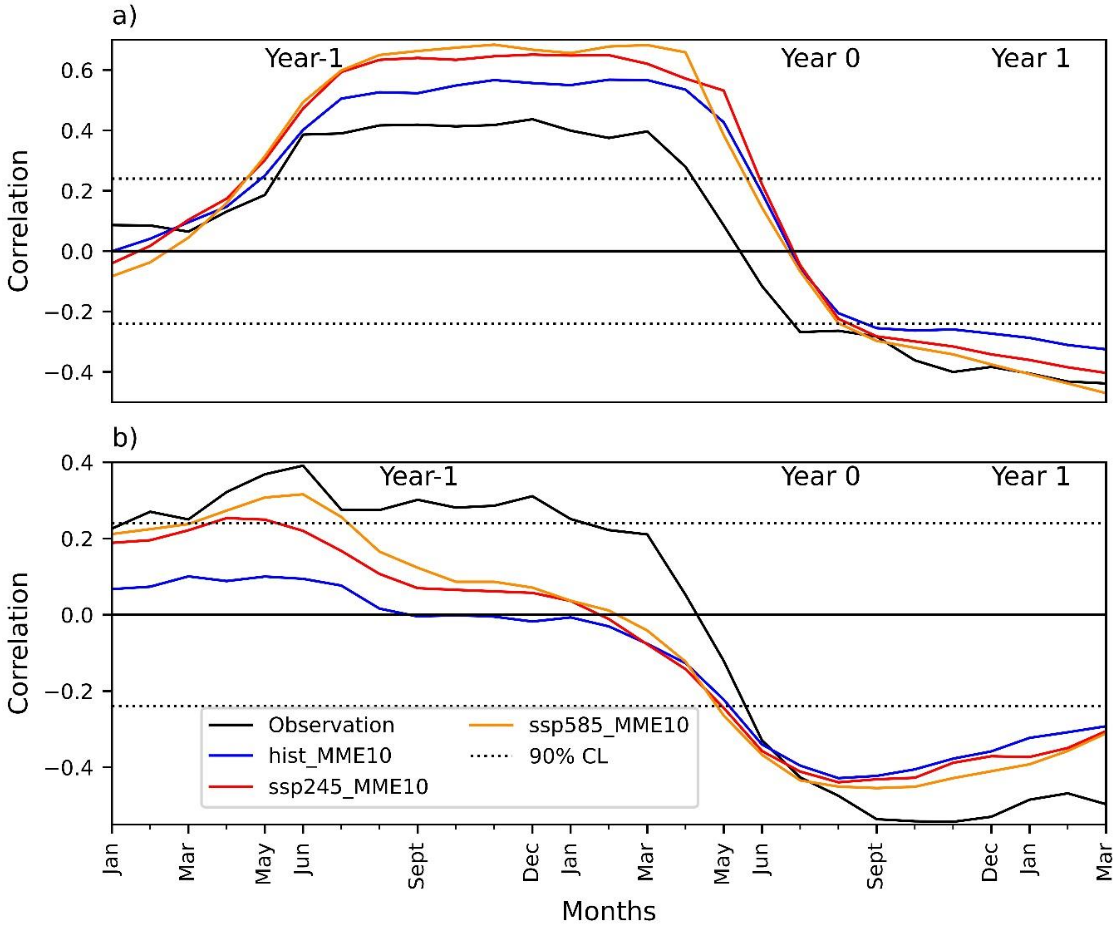

Fig. 6: Lead-Lag association (a) between NTA and ENSO indices and (b) between ENSO and SASM rainfall indices, as depicted using observation, historical, SSP245 and SSP585 scenarios. For both historical and SSPs, the correlations are computed for each selected model and the ensemble mean (MME10) is finally shown. In (a) Lead-lag correlation between the NTA SST Index (based on the normalized PC1 index for MAM season) and monthly Niño3.4 SST Index, starting from the beginning of the previous year (i.e., year−1) to the end of the following year (i.e., year 1). In (b), same as (a), but for the lead-lag correlation between the SASM rainfall index (based on the normalized SASM rainfall index for JJAS season) and monthly Niño3.4 SST Index. The 90% confidence level (CL) based on the bootstrap test is marked in (a-b). The observed analysis used GPCP and HadISST datasets.

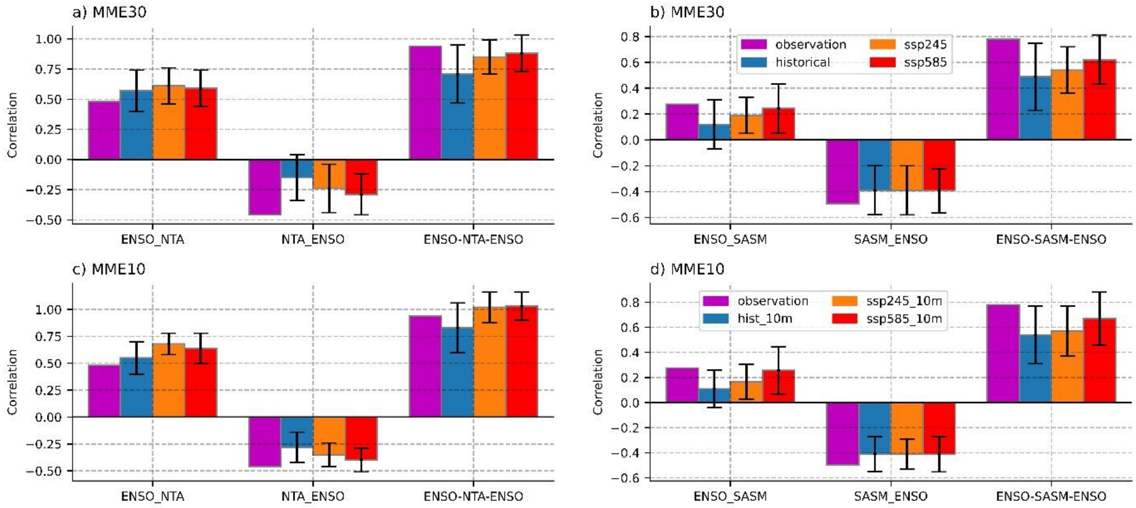

Fig. 7: The correlation between various indices, as presented in (a) considering the mutual NTA-ENSO interactions, as calculated using each of the 30 models and, finally, plotted as an ensemble mean (MME30). Here, ENSO_NTA refers to correlation between Niño3.4 during D(-1)JF(0) and NTA during MAM(0), while NTA_ENSO represents the correlation between NTA during MAM(0) and Niño3.4 during D(0)JF(1). The difference in correlation between ENSO_NTA and NTA_ENSO characterizes the biennial signal in ENSO-NTA teleconnection (denoted as ENSO-NTA-ESNO statistic). In (b), same as (a), but considering the mutual ENSO-SASM interactions. Here the ENSO_SASM statistic refers to the correlation value between Niño3.4 during D(-1)JF(0) and SASM in JJAS(0), while the SASM_ENSO statistic represents the converse relationship, i.e., the correlation value between SASM in JJAS(0) and Niño3.4 during D(0)JF(1). The ENSO_SASM_ENSO statistic is the difference between ENSO_SASM and SASM_ENSO, and characterizes the biennial signal in ENSO-SASM teleconnection. In c) and d) is same as a) and b) but for selected 10 CMIP6 models (MME10). The observed analysis used GPCP and HadISST datasets.

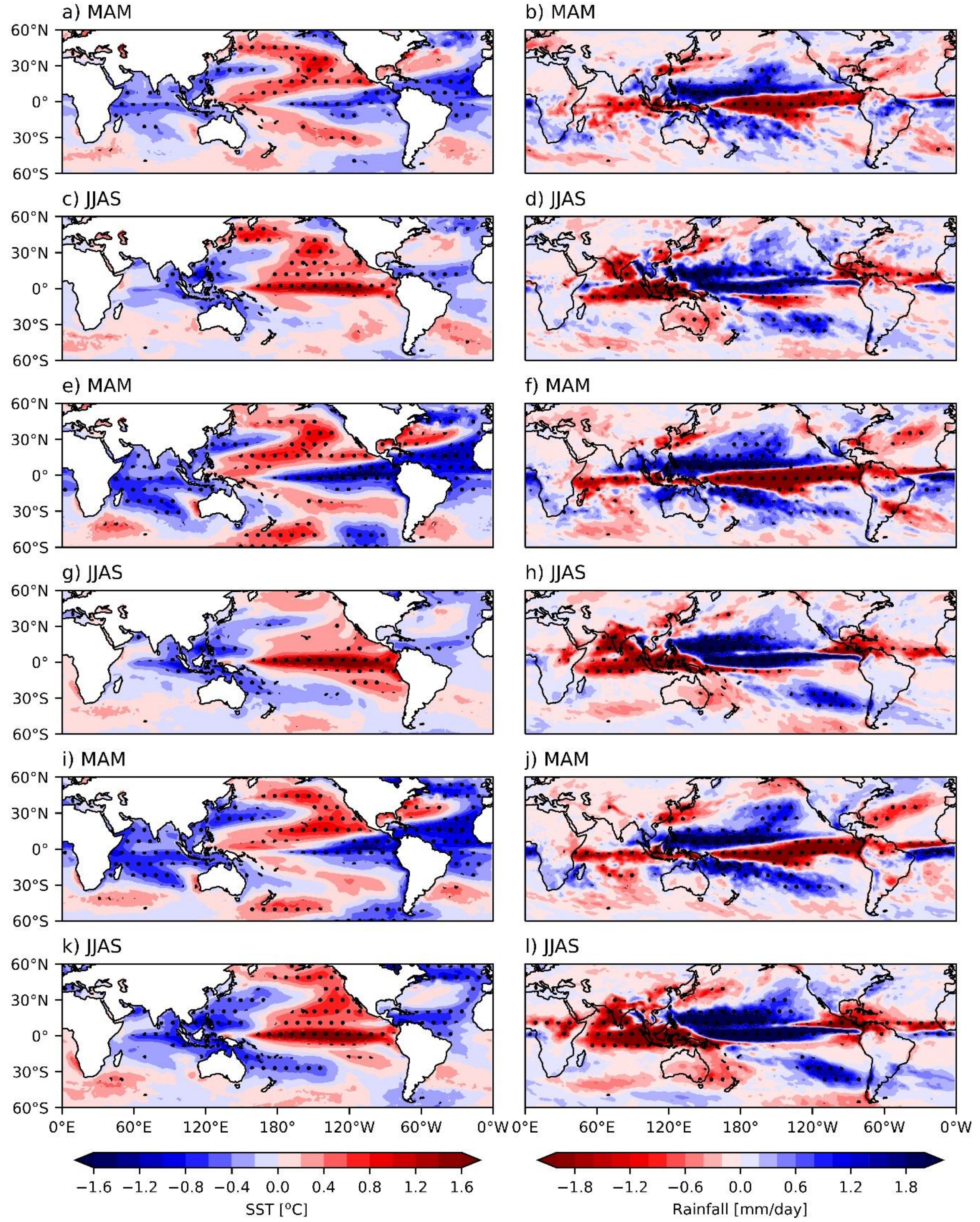

Fig. 8: Composite difference map in SST and rainfall anomalies as computed for MME10 using historical, SSP245 and SSP585 simulations, for the MAM(0) and JJAS(0) seasons. In (a) and (c), the difference between CNTA_ElNino and WNTA_LaNina composites for SST anomalies, using historical simulations. In (b) and (d), same as (a) and (c), but for anomalous rainfall. In (e-h), same as (a-d), but for SSP245. In (i-l), same as (a-d), but for SSP585. The stippling in (a) to (l) represents regions where the composite difference is statistically significant above 95% confidence level as calculated using the bootstrap test.

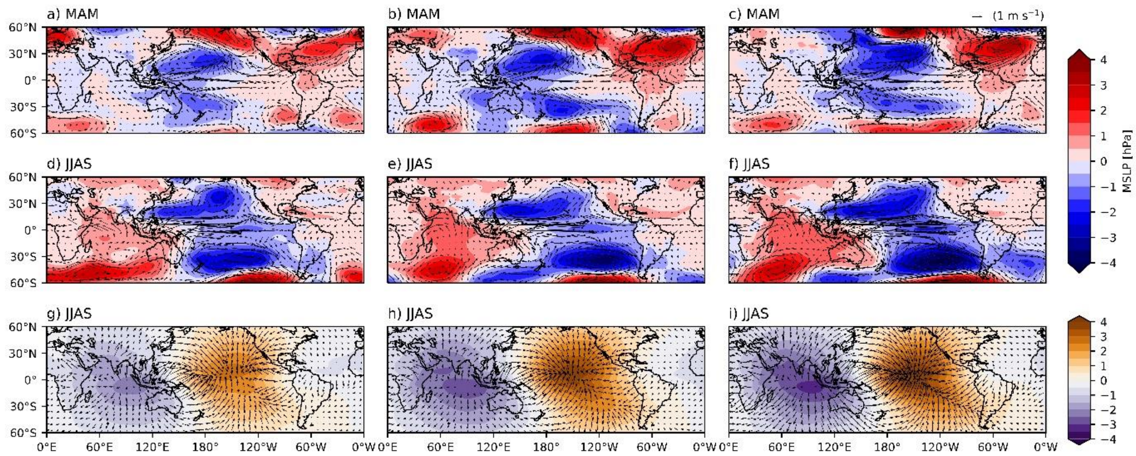

Fig. 9: Composite difference map in MSLP, 850 hPa wind (in vector) and velocity potential anomalies as computed for MME10 using historical, SSP245 and SSP585 simulations. In (a) and (d), the difference between CNTA_ElNino and WNTA_LaNina composites for MSLP and 850 hPa wind anomalies, using historical simulations as computed for the MAM(0) and JJAS(0) seasons. In (b) and (e), same as (a) and (d), but for SSP245. In (c) and (f), same as (a) and (d), but for SSP585 simulations. Composite difference map in Velocity Potential anomalies ($shading,\ \times 10^{6}\ m^{2}\ s^{-1}$) and Divergent wind vector ($m\ s^{-1}$) at 850hPa for JJAS(0), using (g) historical, (h) SSP245 and (i) SSP585 simulations.

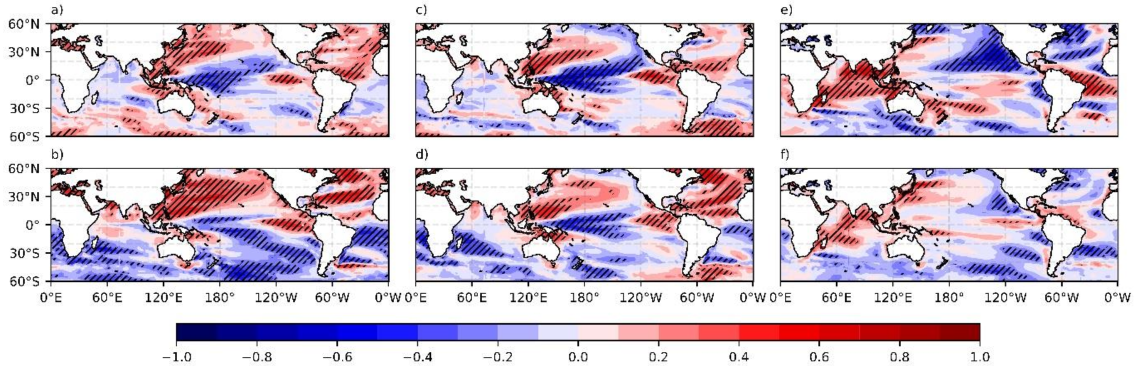

Fig. 10: In (a), Inter-model correlation between the future change in SST under SSP245 and future change in biennial signatures for ENSO-NTA under SSP245 (i.e., refer to ENSO-NTA-ENSO statistic as used in Fig. 7a, c) using all 30 CMIP6 models. In (b), same as (a), but for SSP585. In (c) and (d), same as (a) and (b), but for the inter-model correlation between the future change in SST and future change in SD for ENSO index. In (e) and (f), same as (a) and (b), but for the inter-model correlation between the future change in SST and future change in SD for SASM rainfall index. Note that for future SST change, the relative difference in annual mean SST is used here after removing the zonal mean over the tropics (i.e., between 30°S to 30°N). See Section 2 for the definitions of the NTA, ENSO (Niño3.4) and SASM indices. Also, see Figure 7 captions for more details on ENSO-NTA-ENSO statistics defining the future change in biennial signature in the ENSO-NTA system. Black hatch indicates the correlation values are significantly above 90% using the bootstrap test.

Table

Table1. A list of the CMIP6 models utilized in the study. The names of selected models are highlighted in bold.

Sr. No.	Model Name	Institute	Country	Resolution
1.	ACCESS-CM2	Commonwealth Scientific and Industrial Research Organization	Australia	250 km
2.	ACCESS-ESM1-5	Commonwealth Scientific and Industrial Research Organization	Australia	250 km
3.	BCC-CSM2-MR	Beijing Climate Center	China	100 km
4.	CAMS-CSM1-0	Chinese Academy of Meteorological Sciences	China	100 km
5.	CanESM5	Canadian Centre for Climate Modelling and Analysis	Canada	100 km
6.	CMCC-CM2-SR5	Fondazione Centro Euro-Mediterraneo sui Cambiamenti Climatici	Italy	100 km
7.	CMCC-ESM2	Fondazione Centro Euro-Mediterraneo sui Cambiamenti Climatici	Italy	100 km
8.	CNRM-CM6-1	National Center for Meteorological Research, Météo-France and CNRS laboratory	France	100 km
9.	**CNRM-CM6-1-HR**	National Center for Meteorological Research, Météo-France and CNRS laboratory	France	25 km
10.	**EC-Earth3**	Swedish Meteorological and Hydrological Institute/SMHI	Sweden	100 km
11.	EC-Earth3-CC	Swedish Meteorological and Hydrological Institute/SMHI	Sweden	100 km
12.	**EC-Earth3-Veg-LR**	Swedish Meteorological and Hydrological Institute/SMHI	Sweden	100 km
13.	**FGOALS-f3-L**	Chinese Academy of Sciences	China	100 km
14.	FGOALS-g3	Chinese Academy of Sciences	China	100 km
15.	**FIO-ESM-2-0**	First Institute of Oceanography, State Oceanic Administration	China	100 km

16.	**GFDL-ESM4**	National Oceanic and Atmospheric Administration, Geophysical Fluid Dynamics Laboratory	United States	50 km
17.	GISS-E2-1-G	Goddard Institute for Space Studies	United States	250 km
18.	GISS-E2-1-H	Goddard Institute for Space Studies	United States	250 km
19.	**IITM-ESM**	Centre for Climate Change Research, Indian Institute of Tropical Meteorology	India	250 km
20.	INM-CM5-0	Institute for Numerical Mathematics, Russian Academy of Science	Russia	100 km
21.	IPSL-CM6A-LR	Institute Pierre Simon Laplace	France	100 km
22.	**KACE-1-0-G**	National Institute of Meteorological Sciences/Korea Meteorological Administration	Korea	250 km
23.	MCM-UA-1-0	Department of Geosciences, University of Arizona	United States	250 km
24.	MIROC6	Japan Agency for Marine-Earth Science and Technology	Japan	100 km
25.	MPI-ESM1-2-LR	Max Planck Institute for Meteorology	Germany	250 km
26.	**MRI-ESM2-0**	Meteorological Research Institute	Japan	100 km
27.	NESM3	Nanjing University of Information Science and Technology	China	100 km
28.	NorESM2-LM	Norwegian Meteorological Institute	Norway	100 km
29.	NorESM2-MM	Norwegian Meteorological Institute	Norway	100 km
30.	**TaiESM1**	Research Center for Environmental Changes, Academia Sinica	Taiwan	100 km

Supplementary Figures